Sulphur-based spinel material as a cathode for Magnesium-ion battery

Yashwanth Kutti Pochareddy

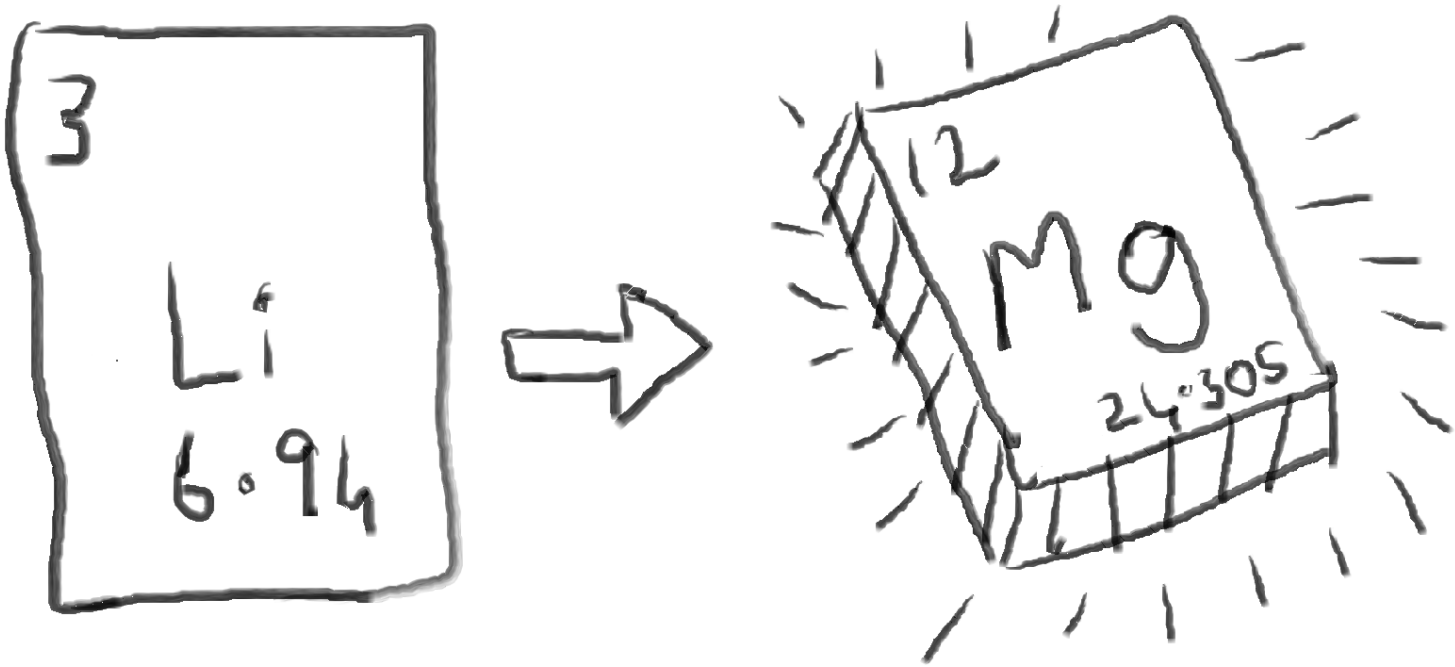

TU Delft

Sulphur-based spinel material as a cathode for Magnesium-ion battery

by

Yashwanth Kutti Pochareddy

to obtain the degree of Master of Science
at the Delft University of Technology,
to be defended publicly on Tuesday June 25, 2019 at 10:00 AM.

Student number:	4739086	
Project duration:	December 17, 2018 – June 25, 2019	
Thesis committee:	Dr. E. M. Kelder,	TU Delft, Supervisor
	Prof. dr. ir. M. Wagemaker,	TU Delft
	Prof. dr. E. H. Brück,	TU Delft
	Dr. ir. A. Vasileiadis,	TU Delft, Mentor

This thesis is confidential and cannot be made public until June 25, 2020.

TU Delft Delft University of Technology

PREFACE

I still remember the first meeting I had with Erik to discuss about available thesis projects. The first few projects were very scary since they all required knowledge of chemistry. Finally, I found the current project which involved proper Material Science and seemed like its worth all risk. Even though with just basic knowledge in chemistry, getting to know the process of finding a new cathode material for a new metal-ion battery was very exciting. In the first few discussions with him, I was very nervous and mixed up words in my sentences, but he patiently listened and made me feel comfortable. I will always remember my Internship evaluation meeting with him, where he encouraged me to speak boldly, and not be shy and was very supportive. Thank you very much, Erik.

Alex, without you I would not have been able to do this thesis. You have helped me in every stage of thesis, helped me understand even the complex parts easily, gave me the freedom to try out new calculations, taught me the concepts patiently even though I did not understand them during first couple of times. Thank you very much for being patient with me.

During the course of my masters, I have made some wonderful friends and a sister, from whom I have learnt a lot. Thank you, guys. I thank my bachelor's professor Dr. Gopinath for involving me in his research right from 2nd year of bachelors and introducing me to the world of energy and material science. Finally, I thank my parents for being very supportive throughout my thesis. I have learnt a lot in these 2 years both about life and courses. Even though, I felt that my engineering background held me back a bit during certain situations of my courses and thesis, the idea of learning something new has always kept me going. Thank you, TU Delft for helping me grow!

Yashwanth Kutti Pochareddy
Delft, June 2019

ABSTRACT

Li-ion batteries have major disadvantages. One of which is the growth of dendrites (in case Li metal based batteries), a major safety issue. In addition to that, Li-ion batteries also use elements such as Co, and Li, which are regionally scarce. Mg-ion batteries are one of the alternatives for Li-ion batteries. However, the electrolyte and cathode materials for Mg-ion batteries, are still in developmental stages.

In this study, the use of a sulphur-based spinel (also known as thiospinel) material as a cathode is explored. After literature review, $MgMn_2S_4$ and $MgTi_2S_4$ were identified as suitable cathode materials. Following which, the $MgMn_2S_4$ spinel is doped with Ti in the place of Mn at different doping ratios and the resulting combinations are evaluated for their stability, average intercalation voltage, volume change, spinel inversion and migration barriers. Two combinations $MgMnTiS_4$ and $MgMn_{0.75}Ti_{1.25}S_4$ are found to be stable with respect to the end members i.e. $MgMn_2S_4$ and $MgTi_2S_4$. Average voltages of 1.702 and 1.527 (vs. Mg/Mg^{2+}) are observed for $MgMnTiS_4$ and $MgMn_{0.75}Ti_{1.25}S_4$. However, spinel inversion is observed in $MgMnTiS_4$. A volume change of 21.2, and 20% is observed in $MgMnTiS_4$ and $MgMn_{0.75}Ti_{1.25}S_4$, respectively.

Contents

LIST OF FIGURES

List of Tables

1

INTRODUCTION

1.1. NEED FOR ENERGY STORAGE

It is known that renewable energy technologies are predicted to cost less than fossil fuel based energy as early as 2020 [11]. However, the production of energy from renewable sources such as wind and solar is not continuous, due to daily and seasonal variations. This would also affect the security of energy supply [12]. One of the solutions is to interconnect electricity grids of different continents. Saudi's plan on exporting the solar power to the EU is an example of one such solution [13]. However, such solutions are not yet economically feasible, even ignoring the political problems that may arise. Another solution would be to develop energy storage technologies for different time scales. Batteries are one of the storage technologies which are capable of storing energy in the time scale of days. Apart from grid balancing, batteries also play a very important role in the electrification of the transportation sector because currently it is dependent on fossil fuels and contributes to 14 % of global greenhouse gas emissions [14].

Even looking beyond current problems, energy storage plays a crucial role in the development of human civilisation. With the development of human civilisation, its energy needs also increase. Keeping this in mind, Nikolai Kardashev in 1964, developed Kardashev scale to measure the civilisation's technological advancement in terms of energy it has at its disposal. He divided the energy needs of civilisation into three classes: Type I (10^{16} W), Type II (10^{26} W), and Type III (10^{36} W). Current human civilisation is classified under Type 0. Type I civilisation would be able to harness all the energy from a nearby star, use and store it for its needs. Such civilisation would be using devices such as Dyson spheres. Type II civilisation would be able to harness the energy of any star in the galaxy. Type III civilisation also called as Universal Civilisation, would be able to harness dark energy, manipulate space-time, etc [15]. Even though such scales of energy look impossible, one thing that is certain is, there is a need for energy storage.

1.2. NEED FOR NEW METAL-ION BATTERIES - IN A NUT SHELL

With an increasing need for energy and its storage, several battery technologies were explored. Out of which, Li-ion and Li-metal based batteries have gained attention owing to their high energy density [16]. Despite their high energy density, they have major disadvantages. One of which is, the Li-ion batteries based on Lithium metal anode has dendrite

growth from uneven Lithium deposition during charge-discharge cycles, leading to short circuits and a major safety issue [16]. Li-ion batteries use elements such as Cobalt (90 % of reserves are concentrated in Congo and Zambia) and Li (most Li reserves are located in South America) which are regionally scarce and this further raises concerns on long term viability of Li-based batteries [17].

Many alternative battery technologies have been proposed over the years and Magnesium-ion batteries are one of them. Magnesium-ion based batteries with Mg as anode have a high volumetric capacity (3833 mAh/cm^3 vs 2046 mAh/cm^3 (Li)) [18], low reduction potential (-2.37 V vs. SHE) [19], high abundance (2.5 % vs. 0.0017 % (Li), of earth's crust)[16], and low price per ton (2260 $ vs. 98000 $ (Li)) [20]. One major advantage of Mg-ion batteries over Li-ion batteries is that they do not form dendrites [20] and hence one can use Mg as anode and can achieve higher capacities than the intercalation anodes [18]. Since Mg is divalent, it also makes up for it's slightly higher atomic mass than Li [16]. The low reactivity of Mg with air, compared to Li, further strengthens its chance to become a successor of Li-based batteries [16].

1.3. CHALLENGES WITH MG-ION BATTERIES

Despite all the advantages of Mg-ion batteries over Li-ion batteries, they are still in developmental stages. Electrolytes and cathode materials for Mg-ion batteries are the main challenges of Mg-ion batteries. In Li-ion batteries, electrolyte generally decomposes at the electrode interface forming solid electrolyte interface (SEI) layer, which protects the electrolyte from further breakdown, while conducting Li^+ ions. However, in Mg-ion batteries, the SEI layer doesn't conduct Mg^{2+} ions and instead acts as a passivating layer. This happens because of high charge on Mg ion which causes the ion to bind strongly with anionic and chelating species, reducing the movement of Mg ions [16].

With respect to the cathode material for Mg-ion batteries, there are fewer cathode options which offer high positive voltages and energy density. The oxide-based materials that are widely used in Li-ion batteries are not suitable for Mg-ion batteries due to high migration barriers and strong electrostatic interactions with the host lattice [9]. In this study, the focus is on the cathode. More about this is discussed in Chapter 2, along with the research question.

1.4. STRUCTURE OF THE REPORT

The report starts of with a review of intercalation cathode materials for Mg, choice of material for this study and the research questions in Chapter 2. In Chapter 3, the methods and the theory behind the methods are described, along with discussions on convergence tests conducted to find the suitable settings for the chosen material. In Chapter 4, convex hull, average intercalation voltage, spinel inversion, volume change, and the migration barrier results of the material studied are discussed. In addition to the results, recommendations for future studies are also presented in Chapter 4. Finally, in Chapter 5, conclusions of the present work are presented.

2

CATHODE MATERIALS FOR MAGNESIUM-ION BATTERIES

The purpose of this chapter is to give an overview of literature where intercalation cathode materials have been explored as a Magnesium host. In Section 2.1, intercalation cathode materials based on transition-metal sulphides such as chevrel, spinel, layered phase materials are reviewed. In Section 2.2, intercalation cathode materials based on oxides, and in Section 2.3 poly-anion based intercalation cathode materials are reviewed. Towards the end of the chapter, the rationale behind choosing Manganese and Titanium as dopant transition metals in sulphur spinels is presented along with the research questions.

2.1. TRANSITION-METAL SULPHIDES

2.1.1. CHEVREL PHASE

Mo_6S_8, a chevrel phase material, is the first intercalation cathode material to show reversible Magnesium storage capabilities [21], with a reversible capacity of 120 mAh/g and 1.2 V. It is a structure where Mo atoms are on the faces of a cube and the S atoms are on the corners of the cube (See Figure 2.1). 3a and 9d sites together form 3D diffusion channels for the transport of Mg^{2+}. Diffusion occurs through inner- and outer-ring sites. 3a site is surrounded by the inner ring and 9d sites are connected with each other through outer-ring. Migration barrier through inner-ring site is 40 meV and through outer-ring site is 570 meV [1]. Aurbach et al. [21] also observed phase transitions due to Mg atoms occupying inner- and outer-ring sites. Good diffusion properties of Mg, in Chevrel phase at room temperature, were attributed to the delocalisation of Mo's orbitals and screening effect provided by S atoms [18]. However, low capacity and voltage of Mo_6S_8, motivated researchers to keep looking for intercalation materials with high voltage and/or capacity.

2.1.2. SULPHUR - SPINELS & LAYERED STRUCTURES

Bruce et al. [22] were the first ones to demonstrate Mg intercalation in Cubic-TiS_2 (Hereinafter referred to as Ti Spinel) structure. They chemically intercalated Mg in to Ti spinel using an organometallic reagent di-n-butylmagnesium [$(C_4H_9)_2Mg$]. Apart from Ti spinel, they have also intercalated Mg into layered-TiS_2, Mn, V, Mo, and W based oxides. They found that the Ti spinel host had highest Mg content (0.25) of all the hosts tested. High Mg

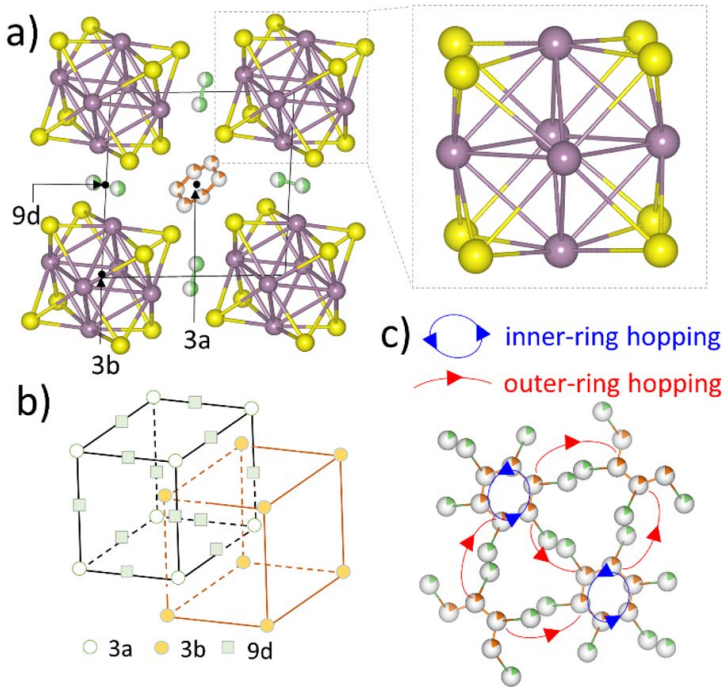

Figure 2.1: Chevrel Phase (a) Mo_6S_8 super anion with highly symmetric 3a, 3b and 9d sites marked (b) Sublattice of 3a and 3b sites (c) Outer- and inner-ring hopping [1]

content in the Ti spinel was explained by the fact that Mg^{+2} is a hard cation and when it co-ordinates with another hard anion such as oxide, it forms a stable association, whereas with sulphides, the interaction is weaker and leads to a high degree of intercalation and mobility. With respect to the layered TiS_2 structure, they found that intercalation is complex and some organic moieties also intercalated along with Mg. In a follow up study, [23], they found that in the intercalated Ti spinel host structure, Mg occupied octahedral 16c sites instead of 8a sites as in a normal spinel. They found that Ti and S occupied their regular 16d and 32e sites, respectively. They have also reported that the lattice parameters increased in a linear fashion with Mg content in the host, due to occupancy of 16c sites. They also noted that the occupancy of Mg in 16c sites was similar to occupancy of Li in 16c sites of Ti spinel [23].

In an effort to find out about the migration barriers of Mg in Ti-based layered and spinel structures, Emly and van der Ven [24] conducted the first DFT study on Layered (O1, O2, P2, and P3) and Spinel structures. They found that Mg likes to occupy octahedral position in O1, O2 and spinel. On evaluating the phase stability of host structures with Mg_xTiS_2 ($0 \leq x \leq 0.5$), they found that O1 layered structure is more stable than all the other structures evaluated. They also found that P2 and P3 structures were better suited for intercalation with large species such as Sodium. When the voltage profiles were evaluated, they found that the Spinel structure exhibits a sloping voltage profile (solid solution). They state that the interactions between Mg^{+2} ions are more likely to be screened in a spinel structure than layered O1 host. O1 layered structure had a migration barrier of 1.16 eV, where as spinel structure had a migration barrier of 0.86 eV (oct → tet → oct). Tetrahedral site in spinel structure was observed to exist in a deeper energy well than O1 structure [1]. They

[1] Deeper energy well here means that barrier to pass through the transition state is higher for O1 structure than the spinel structure

found that the c-lattice parameter has a strong effect on migration barriers both in layered and spinel structures i.e. migration barriers reduced with increase in c lattice parameter.

Following the study of [24], Sun et al. [25] studied the electrochemical cycling and migration barriers of Mg insertion in Ti_2S_4 spinel at 60 °C, with Mg metal as anode and APC as electrolyte. They initally prepared $CuTi_2S_4$, following which Cu was extracted through oxidation and then the material was used a host cathode material. They found that at a cycling rate of C/20, the initial discharge capacity was 200 mAh/g and even with increase in cycling rate up to C/5, the initial discharge capacity did not drop much and remained at 190 mAh/g. During long term cycling tests, the capacity dropped to 140 mAh/g. On doing DFT calculations, they reported that the energy difference between Mg^{2+} occupancy between octahedral and tetrahedral sites was small and could also lead to a disorder across the octahedral and tetrahedral site, which they also confirmed by the XRD study, where, in the intercalated material Mg occupied 30 % of 16c (oct sites) and 20 % of 8a (tet sites) ($Mg[oct]_{0.59}Mg[tet]_{0.189}Cu_{0.1}Ti_2S_4$). They reported that the migration barriers found were slightly lower than [24] and explained that this was due to difference in lattice parameters used.

Following the work of [24] and [25], Liu et al. [9] carried out DFT studies on different transition metal (Ti, V, Cr, Mn, Fe, Co, and Ni) based sulphur spinels as a host for Mg. The term energy above hull (EAH) refers to the driving force of decomposition of the material into its set of most stable materials at that composition. Higher the EAH, lower the thermodynamic stability of the material and vice versa. Figure A.1 illustrates how the EAH of a particular material is calculated. In the charged phase i.e. Mn_2S_4 and Ti_2S_4 spinels were found to have low EAH values compared to other transition metal based sulphur spinels. In the discharged phase, $MgCr_2S_4$, $MgTi_2S_4$, and $MgMn_2S_4$ were found to have low EAH values amongst all the intercalated transition metal suphide spinels. They also found that the site energy difference i.e. the difference in energy when Mg occupies octahedral and tetrahedral positions to be small. This was attributed to the small size of Mg^{2+} ion radius. They also found that Mg in Mn_2S_4, Ti_2S_4, and Cr_2S_4 have migrations barriers 515, 615, 567 meV respectively. Average intercalation voltages of $MgMn_2S_4$, $MgCr_2S_4$, and $MgTi_2S_4$ were found to be 1, 1.65, 0.9 V (vs. Mg/Mg^{2+}) respectively. They concluded that sulphur spinels based on Cr, Mn and Ti are promising cathode materials and that the sulphur spinels have a major advantage of 3D diffusion channels for Mg transport, and low ionic interaction between host and intercalant, due to lower electronegativity of S^{2-}.

In another research [26], Kulish et al. also studied Mg insertion into different transition metal based sulphur spinel hosts through DFT calculations. Similar to [9], Kulish et al. also reported that Mn_2S_4 and Ti_2S_4 are suitable host materials. They also reported that Mg insertion at octahedral site is energetically favorable for Mn, Ti and Fe based spinels. Voltages & diffusion barriers reported by Kulish et al. were also similar to [9], with Mn_2S_4 being an exception. This could be because [9] has not considered 'U 'correction factor in their calculations. More about this is reported in the next chapter (Section 3.3.5). A summary of all the migration barriers of Mg in Ti_2S_4 spinel at conc. vacancy limit is reported in Table 2.1.

2.1.3. OTHER STRUCTURES - MoS_2 & NbS_3

MoS_2 or Molybdenum disulphide is a layered structure (See Figure 2.2). Li and Li [27] first demonstrated the use of MoS_2, a layered material, as an Mg host cathode material. They found that the capacities and charge/discharge efficiencies varied between 2 - 25 mAh/g

Table 2.1: Migration barriers reported for Ti based spinel in different studies

Reference	Migration barrier (meV)	Path
[24]	860	(oct → tet → oct)
[25]	~600	(oct → tet → oct)
[9]	~615	(oct → tet → oct)
[26]	~700	(oct → tet → oct)

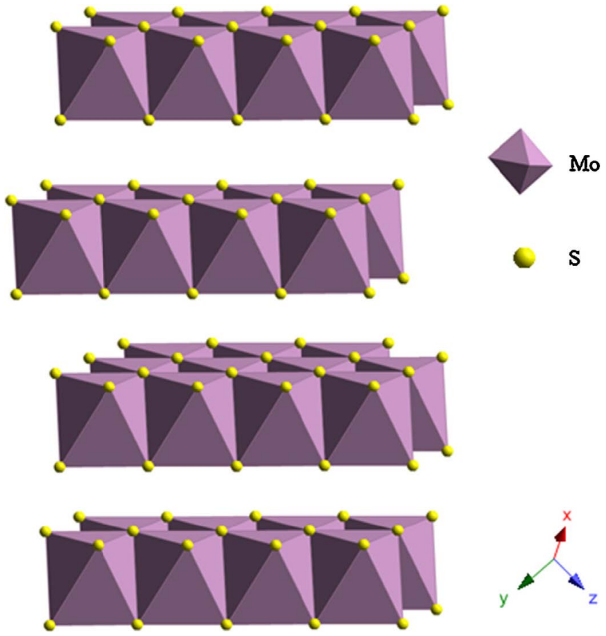

Figure 2.2: Structure of MoS_2 [2].

and 10 - 40%, respectively, in the cells they tested. Liu et al. [28] in an effort to improve the capacities, tested a MoS_2/C, a graphene like composite (with 46.06% C content), and achieved a capacity of 118.8 mAh/g after 20 cycles. In another study [29], graphene like MoS_2 as cathode and 2.5 nm sized particles of Mg were used as anode were tested. They observed a high operating voltage of 1.8 V and a capacity of 161.5 mAh/g after 50 cycles. Shuai et al. [30]in a DFT (Density Functional theory) Nudged Elastic Band (NEB) study found that the migration barrier for Mg^{2+} is 1.12 eV (oct → tet → oct). They also noted that Mg preferred octahedral position, and diffusion path is independent of layer spacing in MoS_2.
Yuan and Günter [31] in 1995 tried Mg intercalation in monoclinic NbS_3 and found that the structure changed even at low current density and also observed that the all the intercalated Mg may not have been removed completely during charging and hence concluded that NbS_3 may not be a suitable cathode material for Mg-ion batteries.

2.2. TRANSITION-METAL OXIDES

2.2.1. OXIDE SPINELS

Liu et al. [8] conducted a DFT study to find out the average intercalation voltages, and migration barriers of Mg in TM_2O_4, where TM = Ti, V, Cr, Mn, Fe, Co, and Ni. They observed

the following voltage trend: Fe > Cr > Ni > Co > Mn > V > Ti. A similar trend was also observed in sulphur spinels [9]. They also found that the volume change of the structure was the lowest for Ti_2O_4 and V_2O_4 host materials. All the hosts were found to be thermodynamically stable in the discharged phase, where Mn_2O_4 showed highest stability in discharged phase, followed by Co_2O_4 and Ni_2O_4. They also evaluated the thermal stability at high temperatures and found that Ti, V, Cr, and Mn based oxide spinels exhibited superior thermal stability than others. On performing NEB calculations to find the migration barriers for Mg in Mn_2O_4, Co_2O_4, Cr_2O_4, and Ni_2O_4, they found that migration barriers were in the range of 600 - 800 meV with Mg in Cr_2O_4 having lowest migration barrier. Finally, they concluded that Mn_2O_4 is a good cathode host with Mg as intercalant, despite the high migration barrier.
In another study [32], researchers from the same group, conducted DFT NEB calculations to see what governs the migration barriers. They have found that inserting the Multivalent (MV) Cation in a site that it does not prefer would reduce the migration barrier compared to inserting the MV cation in a site it prefers. Mg^{2+} prefers six coordination i.e. octahedral site. So inserting the Mg^{2+} cation in octahedral site (16c site) would increase the migration barrier compared to insertion in 8a site. The same was confirmed DFT NEB calculations done on host Mn_2O_4 spinel structure. In addition to that, they have suggested that MV cation in sulphide based host would comparitively perform better in terms of migration barriers albeit with decrease in voltage.

2.2.2. MoO_3

MoO_3 is a double layered structure (See Figure 2.3). MoO_3 when used as a cathode against

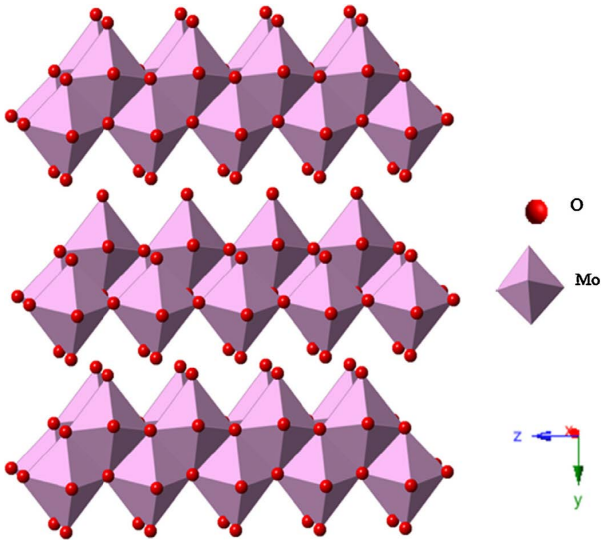

Figure 2.3: Structure of MoO_3 [2].

an Mg metal anode, an open circuit voltage of 2.28 V vs. Mg/Mg^{2+} and a capacity of 143 mAh/g was observed [33]. It was also previously discussed by Bruce et al. [22] that a maximum of 0.05 Mg content was intercalated into MoO_3 host yielding $Mg_{0.05}MoO_3$. However, Gregory et al. [33] reported that a maximum of $Mg_{0.5}MoO_3$ could be achieved. Wan et al. [34] to improve the performance, doped the structure with Fluorine to improve the electronic conductivity of the structure, and observed a reduction in migration barrier from

0.9 eV to 0.49 eV. Further testing the material in a cell, yielded a capacity of 70 mAh/g. In addition to the discrepancies mentioned about maximum intercalated Mg content, the capacity reported by [33] is also different from the capacity reported by [35]. Nevertheless, the stronger and rigid oxide bonds of MoO_3 may result in more structural damage during cycling [2].

2.2.3. V_2O_5

V_2O_5 is a layered crystalline structure with V^{5+} ions are coordinated with 5 oxygen and the intercalant occupies the space between the layers (See Figure 2.4) [18]. Migration barriers of 620 meV and 1000 meV were observed for δ and α polymorphs of the structure respectively [36]. Since, the structure has two polymorphs, a transition from α to δ was observed upon Mg insertion [3]. δ phase was found to be exhibit good properties i.e. average voltage (2.56 V), lower migration barrier (760 meV). However, δ phase was found to be metastable at room temperature in deintercalated limit, while α phase was stable. Due to this, no experiments were carried out on δ-V2O5 till date [18], but with α phase based nanocrystalline structured cathode and α phase based thin film cathode were reported by Amatucci et al. [37] and Gershinsky et al. [38], respectively.

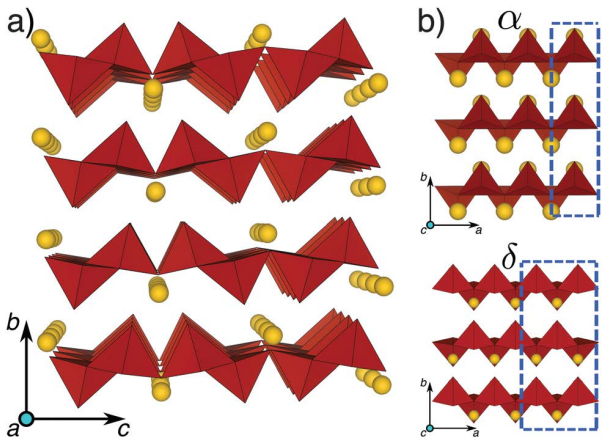

Figure 2.4: (a) V2O5 structure with α and δ polymorphs in b-c plane. (b) Dashed lines showing the difference in stacking of layers of α and δ polymorphs on a-b plane [3].

2.3. POLY-ANION BASED

2.3.1. PHOSPHATES

Poly-anion based compounds have 1D diffusion channels. Mg^{2+} ions in olivine $FePO_4$ structure travel along a zig-zag path from oct sites to tet sites. Conc. vacancy limit diffusion of Mg in $FePO_4$ yielded migration barrier of 580 meV. On the other hand, at exactly half conc. vacancy limit i.e. $Mg_{0.5}FePO_4$, a diffusion barrier of 1025 meV was observed, indicating that it is difficult to remove the Mg ion from the structure [39]. On testing the material in a cell, only 12 mAh/g capacity was observed, which is only 6 % of its theoretical capacity [39]. This was attributed to surface amorphization, which prevented the electrochemical reaction from penetrating the bulk.

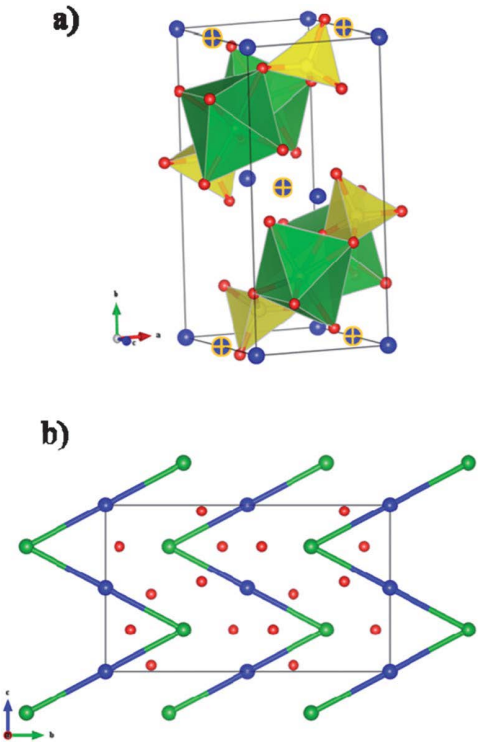

Figure 2.5: (a) Olivine structure. (b) 2D view along (100) plane. Red = Oxygen; Yellow = Si/P; Green = Transition metal (4c site); Blue = Mg (4a site) [4]

2.3.2. SILICATES

Chen et al. [40] tested $MSiO_4$ (M = Ti, V, Cr, Mn, Fe, Co, Ni, Cu, Zn) as a host structure for Mg. They found that migration barriers were in the range of 450 - 770 meV. The lowest migration barrier was observed in CrSiO4 host structure. Orikasa et al. [41] tested Mg as an intercalant in the tetrahedral site of the host $FeSiO_4$, and found that it provided a reversible capacity of 330mAh/g at 2.5 V. Measurements were done at 6.62 mA/g current density and 55°C. The superior performance was attributed to Mg occupying the tetrahedral sites [41], which Mg doesn't prefer. This is also inline with the discussion by [32]. Zheng et al. compared the capacities, of $MgCoSiO_4$ cathode under difference preparation methods. They found that the cathode prepared using a solvo-thermal approach performed better compared to others, with a capacity of 167 mAh/g at 0.1C.

2.4. RESEARCH QUESTION

Table 2.2 presents the Migration barrier for Mg^{2+} in different structures. It can be observed that the sulphur based spinels have the lowest migration barriers among all the structures listed. This is due to the presence of 3D diffusion channels, volume expansion, and the lower electronegativity of S^{2-} than O^{2-} [9]. The effect of reduced electronegativity can be seen from Table 2.2, where Mn based suphur spinel has lower migration barrier than Mn based oxide spinel. Therefore, sulphur based spinel ($MgTM_2S_4$ - TM is transition metal) has been chosen for this study. In addition to that, Rong et al. [32] et al. in their study also found that placing the Multivalent intercalant (Here Mg^{2+}), in a site it does not prefer will reduce the migration barrier. Hence, in this study the Mg atoms will be placed in the tetra-

hedral (8a) sites. With respect to the transition metals in the sulphur spinel, Manganese, Titanium and Chromium based sulphur spinels were found to be thermodynamically stable. Hence, for further study, Mn and Ti has been chosen. Chromium based sulphur spinel is not included in the study due to Cr's proven carcinogenic effects [42].

Table 2.2: A summary of migration barriers for Mg^{2+}, in different hosts

Structure	Migration barrier (meV)
Mo_6S_8 (Chevrel phase)	570 [1]
TiS_2 (Layered)	1160 [24]
Ti_2S_4 (Spinel)	~615 [9]
Mn_2S_4 (Spinel)	~515 [9]
MoS_2 (Layered)	1120 [30]
NbS_3	Not reported
Mn_2O_4 (Spinel)	~850 [8]
MoO_3 (Layered)	~880 [34]
V_2O_5 (Layered)	~1000 [3]
$FePO_4$ (Olivine)	1025 [39]
$CrSiO_4$ (Olivine)	~450 [40]
$TiSiO_4$ (Olivine)	~660 [40]
$MnSiO_4$ (Olivine)	~770 [40]

In this study, the focus will be on developing a new cathode material for Magnesium-ion battery. To do this, Mn based sulphur spinel i.e. $[\ ]Mn_2S_4$ will be doped with Ti, and the stability, voltage, volume change, inversion, and the migration barriers of the resulting doping combinations are evaluated. Therefore, the research question can be stated as follows:

What would be the effect of doping Manganese based sulphur spinel with Ti or vice versa, on the performance of the resulting combinations, namely:

- **Thermodynamic stability,**
- **Average intercalaion voltage (vs. Mg/Mg^{2+}),**
- **Change in the volume of structure after intercalation,**
- **Inversion of the Spinel, and**
- **Migration barrier for the Mg^{2+}**

3

METHODS

In this chapter, methods and procedure used in the current study are discussed. In Section 3.1, the theory behind DFT calculations is briefly discussed. Following which, in Section 3.2 the procedure of setting up DFT calculations is explained. In Section 3.3, convergence tests conducted to find the input parameters for the study are discussed, and in Section 3.4, the process of creating doping combinations is discussed. Finally, in Section 3.5, a brief overview of theory behind the Nudged Elastic Band (NEB) method and the procedure of setting up a NEB simulation to find the migration barrier is provided.

3.1. THEORY

It is of our interest to find the properties of a given material which is made up of several atoms. The energy of the atoms, and how it changes with the movement of atoms is one of the fundamental things that we would like to know. To know the location of an atom, its nuclei and electrons' location must also be known. It is known that the mass of atomic nuclei is much greater than the mass of the individual electrons, in an atom (Equation 3.1). This means that the electrons respond to changes in their surroundings much faster than the nuclei. As a result, the physical question can be split into two parts. First, the equations describing the electron motion are solved, keeping the atomic nuclei fixed. For a given set of electrons moving in the field of a fixed set of nuclei, the lowest energy configuration/state of electrons is found [43]. This lowest energy state is known as ground state energy of the electrons, and the splitting of the nuclei and electrons in two parts i.e. fixed and moving is known as Born-Oppenheimer approximation [44].

$$m_{nuclei} >> m_e \tag{3.1}$$

A simple form of Schrödinger equation is $H\psi = E\psi$, in which H is Hamiltonian operator and ψ is a set of solution/eigen states of the Hamiltonian. Each of the solution, ψ_n has an eigen value associated with it i.e. E_n that satisfies the eigen equation. The Schrödinger equation that describes our case i.e. multiple electron interacting with multiple nuclei is (Equation 3.2) [43]:

$$\left[-\frac{h^2}{2m_e} \sum_{i}^{N_e} \nabla_i^2 + \sum_{i}^{N_e} V_{ext}(r_i) + \sum_{i}^{N_e} \sum_{j>1} U(r_i, r_j) \right] \psi = E\psi \tag{3.2}$$

Where, the first term in the square brackets defines kinetic energy of each electron, the second term describes the interaction energy between each electron and a collection of atomic nuclei, and the third term describes the interaction between different electrons. For the Hamiltonian in Equation 3.2, ψ is the electronic wave function. ψ is a function of each of the spatial coordinates of each of the N electrons[1] and E is the ground state of the electrons:

$$\psi = \psi(r_1, r_1, ..., r_N) \tag{3.3}$$

ψ in Equation 3.3 can also be written as the product of individual one-electron functions of N electrons (Equation 3.4) i.e. the electron wave functions are separated.

$$\psi(r_1, r_1, ..., r_N) = \psi_1(r)\psi_2(r), ..., \psi_N(r) \tag{3.4}$$

This is known as the Hartree product. The approximation is done because in an atom, the number of electrons, N, is much larger than the number of nuclei. For example, if we are interested in CO_2 molecule (22 electrons), then the full wave function is 66-dimensional function. This number increases, even more, when atoms with a higher number of electrons are considered and solving the Schrödinger equation gets complicated faster due to the higher number of dimensions. This situation worsens when we look at the Hamiltonian term in Equation 3.2, because the third term in it is an electron-electron interaction, and the individual electron wave function, $\psi_i(r)$, cannot be found without simultaneously considering individual electron wave functions of all other electrons. Therefore, this means that the Schrödinger equation is a many-body problem.
Even though the Schrödinger equation can be seen as a fundamental quantum mechanics problem, its worth noting that the wave function for any particular set of coordinates cannot be directly observed. What can be measured is the probability that N electrons are at a particular set of coordinates $(r_1, r_2, .., r_N)$[43]. This probability is equal to:

$$n(r) = \psi^*(r_1, r_2, r_3...r_N)\psi(r_1, r_2, r_3...r_N) \tag{3.5}$$

where, asterisk indicates a complex conjugate and n(r) is the density of electrons at a particular position in space. The density of electrons can also be rewritten as:

$$n(r) = 2\sum_i \psi_i^*(r)\psi_i(r) \tag{3.6}$$

From this point on Density Functional Theory (DFT) is introduced. The heart of DFT is based on two fundamental theorems i.e. Hohenberg and Kohn theorems.
Theorem 1 states that the ground state energy is a unique functional[2] of electron density (Equation 3.7). This is why the theory is known as density functional theory (DFT). Ground-state electron density can uniquely determine all properties, including energy and the wave function of the ground state. This means the Schrödinger equation can be solved i.e. the ground-state energy can be found by finding electron density, a function of three spatial variables, rather than using wave function (a function of 3N variables). Thus the problem is reduced from 3N dimensions to 3 dimensions[44].

$$E = E[n(r)] \tag{3.7}$$

[1] This means the equation describes the location of all the electrons present in all the directions
[2] Means a function of function. An example is Integral $\left(F[f] = \int_{-1}^{1} f(x)dx\right)$.

Theorem 2 states that the electron density that minimizes the energy of overall functional is the true ground state electron density corresponding to the full solution of Schrödinger equation (Equation 3.8).

$$E[n(r)] > E_0[n_0(r)] \tag{3.8}$$

Energy functional (Equation 3.9) can be divided into two main parts i.e. the one that is known and the other one that is not known. The known part (Equation 3.10) has kinetic energy, coulomb interaction between electrons and nuclei, the coulomb interaction between a pair of electrons, and the coulomb interaction between a pair of nuclei terms (from left to right). The unknown part includes all quantum mechanical effects that are not included in the 'known' term and is known as exchange-correlational functional (will be called further as XC-functional).

$$E[\{\psi_i\}] = E_{known}[\{\psi_i\}] + E_{XC}[\{\psi_i\}] \tag{3.9}$$

Where,

$$E_{known}[\{\psi_i\}] = -\frac{h}{m_e}\sum_i \int \psi_i^* \nabla^2 \psi_i d^3r + \int V(r)n(r)d^3r + \frac{e^2}{2}\iint \frac{n(r)n(r')}{r-r'} d^3r d^3r' + E_{ion} \tag{3.10}$$

Until now, the discussion is only about simplifying the calculation instead of fully solving the Schrödinger equation for wave function. Kohn and Sham showed that the correct electron density can be found by solving a set of equations in which each equation involves only one electron:(Equation 3.11).

$$\left[-\frac{h}{2m}\nabla^2 + V(r) + V_H(r) + V_{XC}(r)\right]\psi_i(r) = \epsilon_i(r)\psi_i \tag{3.11}$$

The difference between Kohn-Sham equation (Equation 3.11) and full Schrödinger equation (Equation 3.2) is that there is no summation term in Kohn-Sham equation. This is because the solution for Kohn-Sham equations are single-electron wave functions, which only depend on three spatial variables $\psi_i(r)$[6].
Inside Equation 3.11, there are three potentials V, V_H, and V_{XC}. V_H is hartree potential and V_{XC} is exchange-correlation potential $\left(V_{XC} = \frac{\delta E_{XC}}{\delta n(r)}\right)$. This leads to circular loop where to solve Kohn-Sham equation, V_H has to be defined, to define V_H we need $n(r)$, to know $n(r)$ we need to know single-electron wave functions, and to know this we need to solve Kohn-Sham wave functions [43]. To break the loop, an initial $n(r)$ is defined and then the steps are carried out as shown in Figure 3.1.

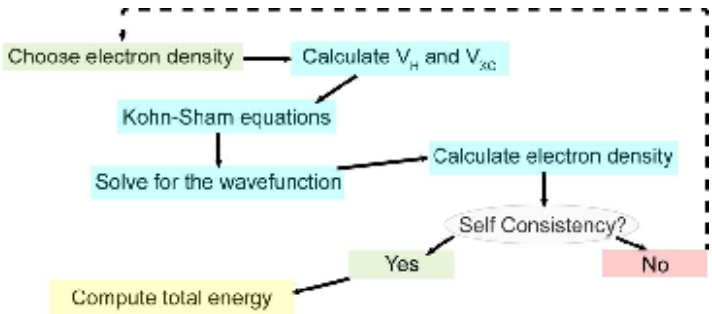

Figure 3.1: Self-Consistency Loop [5]

The ground state can be found by minimizing the energy functional (Equation 3.9), and this is done by finding a self-consistent solution to single-particle equations. However, the catch is that the exchange correlational-functional, $E_{XC}[\psi_i]$ must be specified. But from Equation 3.9 and Equation 3.10 it can be understood that it is difficult. Fortunately, there is one case, $E_{XC}[\psi_i]$ can be derived from the uniform electron gas. In uniform electron gas, the electron density, $n(r)$, is constant at all points in space [43]. XC potential at a point is set as shown in (Equation 3.12).

$$V_{XC}(r) = V_{XC}^{\text{electron gas}}[n(r)] \tag{3.12}$$

This approximation uses only the local density to define XC-functional. Hence, this method is known as LDA. However, this is not the only functional. There are several other functionals such as GGA, PW91, PBE, B3LYP, etc. In addition to that of local density, local electron density gradient is also considered in GGA. Hence, the name generalized gradient approximation. Even though GGA considers the electron density gradient, it doesn't give much physical information than LDA. Therefore, even GGA is not accurate enough. However, this served as a groundwork to develop other functionals such as Perdew-Wang (PW91), Perdew-Burke-Ernzerhof (PBE) functionals. PBE considers local electron density, gradient, and the second-order gradient in the enhancement factors F(x) and F(c). PBE is proven to be highly accurate and most widely used. Hence, this functional is used in the current study. Hence, the pseudopotentials of PBE are considered for the study. These pseudopotentials are present for each element and in the form of POTCAR files [6].

Once the electronic ground state is obtained, forces on the ions can be easily obtained because the $\hat{H}$ is known and the correct wave functions are known because the right density functional/right electron density is also known. This is done using Equation 3.13 [44].

$$F_I = -\frac{dE}{dr_I} = -\left\langle \psi_i \left| \frac{\partial \hat{H}}{\partial r_I} \right| \psi_i \right\rangle \tag{3.13}$$

The relaxation of ions is done using the IBRION tag, which will be discussed in the next section.

Now the discussion is about how the functions are considered for the elements in the system. The word pseudo means artificial. To mimic the actual potentials of the elements, pseudopotentials are created. Pseudopotentials are created by dividing electrons into two groups. One where the nucleus is frozen along with the core electrons and the rest of the electrons are pseudized to create wave functions. This is done to reduce the number of electrons considered in the system. When atoms get together to form solid, the core electrons stick together tightly to their nucleus in a deep potential well and remain unchanged in most circumstances. They get localized and they don't notice whether they are in a solid or in an atom. These electrons also neutralize the nucleus charge as shown in the Figure 3.2. The electrons apart from core electrons are valence electrons. These electrons are the ones that interact with other materials, form bonds, conduct electricity, etc [6].
The separation of frozen core electrons + nucleus and valence electrons is done to reduce the computational load. When the wave function of valence electrons passes through the localized core electrons, it oscillates rapidly and has many nodes (Figure 3.3). Presence of the nodes will increase the complexity of wave function. To remove the nodes, this feature of the curve is 'softened'. This procedure is called pseudization. From ??, it can be seen that there is a parameter called r_c, critical radius. Depending on the choice of this value,

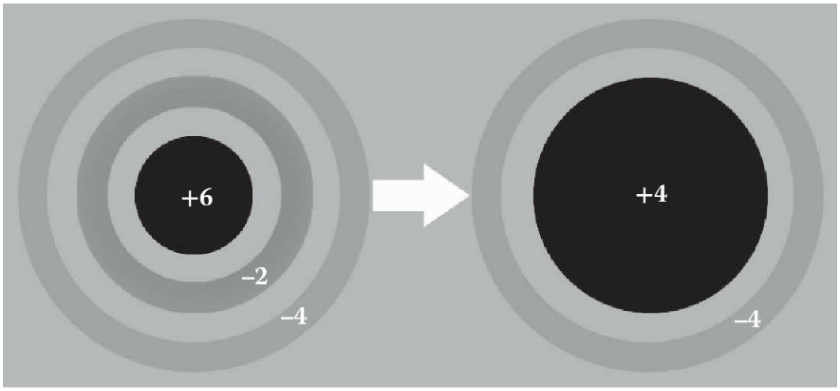

Figure 3.2: An example of carbon showing frozen core and valence electrons for the construction of its pseudopotential [6]

the accuracy of pseudopotentials varies. With small r_c, the accuracy is higher because a higher number of valence electrons are considered and can mimic the potentials well [6]. However, the computation time also increases.

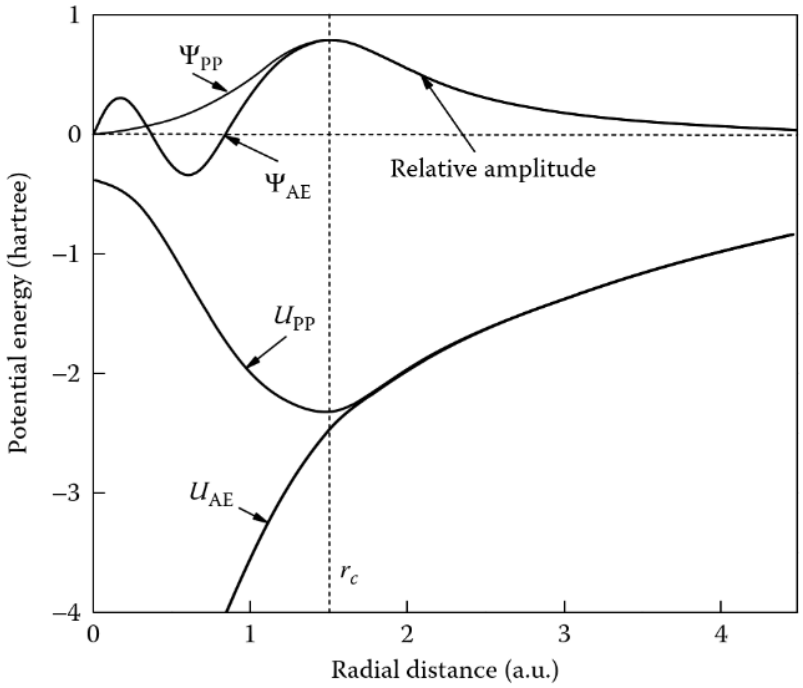

Figure 3.3: Illustration of all-electron (ψ_{AE}) and pseudo (ψ_{pp}) wave functions and the corresponding all-electron (U_{AE}) and pseudo (U_{PP}) potentials [6]

Based on this, there are two pseudopotentials: US-pp (Ultra-soft) and PAW-pp (Projector Augmented Wave). The difference between PAW-pp and US-pp is that in US-pp r_c is larger than PAW-pp and PAW-pp reconstructs the exact valence wave functions with all the nodes in the core region. PAW-pp is a frozen core All-Electron potential approach. An example wave function of PAW is illustrated in Figure 3.4. ψ_{core} is the core electron wave function, ψ_{inter} is the valence electron wave function, and ψ_{net} is the overlapping part of ψ_{core} and ψ_{inter}. ψ_{net} is removed from the final wave function to better represent the all-electron wave function. In PAW-pp's, due to the use of ψ_{core}, the core part is well reproduced and

doesn't need many Projector Waves and hence can give greater accuracy with less computational effort [6].

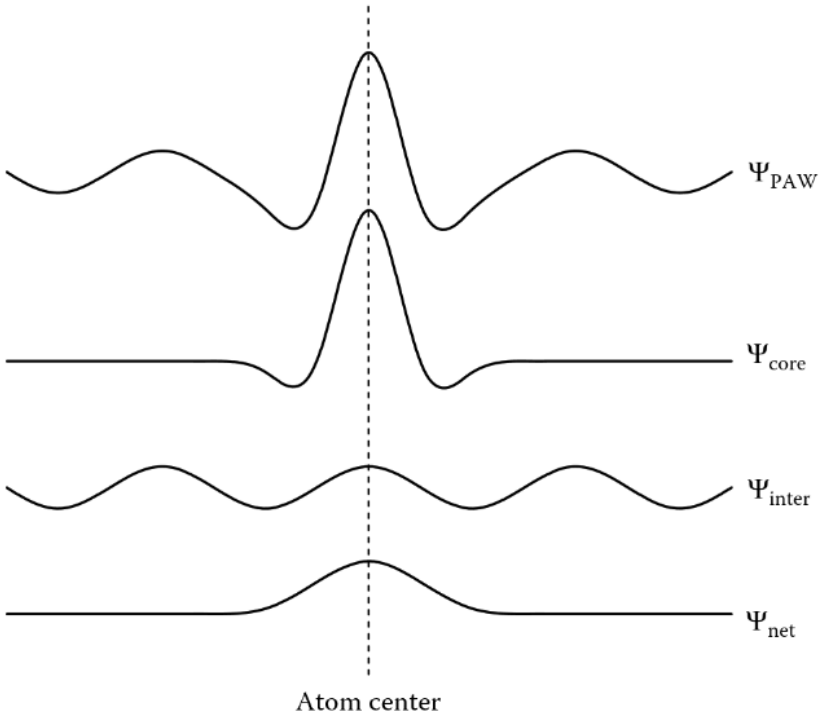

Figure 3.4: Illustration of Projector Augmented Wave construction [6]

3.2. PROCEDURE

Vienna Ab initio Simulation Package or VASP has been used for performing DFT calculations. In this section, a detailed explanation of the inputs to VASP, & choice of inputs is provided.

VASP needs 4 input files (INCAR, KPOINTS, POSCAR, and POTCAR, where CAR means 'card' [45]) and it generates several output files depending on the tags set in the INCAR input file (See Table 3.1). An example of all the input files is shown in Figure 3.5.

- **INCAR** - INCAR file is the central input file and it has several tags, which tells VASP on how to proceed with calculations [46]. An example INCAR file with several inputs is shown in Figure 3.5a and the inputs are explained in Table 3.1.

- **KPOINTS** - KPOINTS file contains information about the mesh-size and the type of grid [47]. Mesh size is dependent on the lattice parameters. More information about how the mesh size is calculated in given in Section 3.3.1. Higher the mesh size, higher the accuracy but at the expense of computation time.

- **POSCAR** - POSCAR file contains the information about the atoms, ionic positions, and lattice geometry of the structure being studied [48]. POSCAR files are usually created from files with '.xsd '/'.cif ' extension. For the present study, $Fd\bar{3}m$ space-group structures in the '.cif 'file format were obtained from the Materials Project ($MgMn_2S_4$ & $MgTi_2S_4$). Spinels have a general formula of $A_{tet}[B_2]_{oct}X_4$, where A

refers to cations occupying tetrahedral (8a) sites, B refers to cations occupying octahedral (16d) sites, and X refers to anions located at 32e sites of a cubic structure which belongs to the space group $Fd\bar{3}m$ [49]. In this study, A is Magnesium, B = transition metals Mn/Ti, X is sulphur. Since this study involved transition metal based suphide spinel structure, general formula can be written as $Mg_{tet}[TM_2]_{oct}S_4$, where TM = Mn/Ti. The unit cell used in this study has 8 Mg atoms in 8a sites, 16 Mn/Ti atoms in 16d sites, 32 S atoms in 32e sites. The unit cell's downloaded have 8 Magnesium atoms, 16 transition metal atoms (Mn/Ti), and 32 Sulfur atoms. Unit cell has been chosen over primitive cell to have more flexibility while creating doping combinations because primitive cells have less number of atoms.

- **POTCAR** - POTCAR file contains the pseudopotential (pp) information of each atomic species in the structure. Each atomic species has a different POTCAR file. POTCAR files of different atomic species have to combined into a new POTCAR file since VASP can only accept one POTCAR file. New POTCAR file must have pseudopotentials in the same order as of the atomic species in the POSCAR file [50].

```
[ypochareddy@hpc11:MgMn2S4]$ more INCAR
ENCUT = 520
ISTART = 0
ICHARG = 2
PREC = Accurate
NSW = 1000
ISIF = 3
IBRION = 2
LREAL = Auto
ISMEAR = -5
NPAR = 4
ISYM = 0
LWAVE = .FALSE.
LCHARGE = .FALSE.
ISPIN = 2
MAGMOM = 8*0.6 16*5 32*0.6 #Mg Mn S
LDAU = .TRUE.
LDAUL = 2 2 2 #Interactions ON if 2
LDAUU = 0.0 4.0 0.0 #Ueff values Mg0 Mn4 S0
LDAUJ = 0.0 0.0 0.0
LDAUTYPE = 2
LMAXMIX = 4
LASPH = .TRUE.
LDAUPRINT = 1
```

(a) An example of INCAR file

```
[ypochareddy@hpc11:k555]$ more KPOINTS
Monkhorst-Pack
 0
Monkhorst-Pack
 5 5 5
 0 0 0
```

(b) An example of KPOINTS file

```
MgMn2S4_Computed MgMnS
  1.000000
 10.309440      0.000000      0.000000
  0.000000     10.309440      0.000000
  0.000000      0.000000     10.309440
       8       16       32

  0.000000      0.000000      0.500000    Mg
  0.000000      0.500000      0.000000    Mg
  0.500000      0.500000      0.500000    Mg
  0.500000      0.000000      0.000000    Mg
  0.750000      0.250000      0.250000    Mg
  0.750000      0.750000      0.750000    Mg
  0.250000      0.250000      0.750000    Mg
  0.250000      0.750000      0.250000    Mg
  0.125000      0.125000      0.125000    Mn
  0.125000      0.625000      0.625000    Mn
  0.625000      0.125000      0.625000    Mn
  0.625000      0.625000      0.125000    Mn
  0.875000      0.375000      0.625000    Mn
  0.875000      0.875000      0.125000    Mn
  0.375000      0.875000      0.625000    Mn
  0.375000      0.625000      0.875000    Mn
  0.375000      0.125000      0.375000    Mn
  0.875000      0.625000      0.375000    Mn
  0.625000      0.875000      0.375000    Mn
  0.625000      0.375000      0.875000    Mn
  0.125000      0.875000      0.875000    Mn
  0.875000      0.125000      0.875000    Mn
  0.375000      0.375000      0.125000    Mn
  0.125000      0.375000      0.375000    Mn
  0.113145      0.113145      0.886855    S
  0.886855      0.386855      0.386855    S
  0.886855      0.886855      0.886855    S
  0.386855      0.613145      0.113145    S
  0.613145      0.886855      0.613145    S
  0.886855      0.113145      0.113145    S
  0.386855      0.886855      0.386855    S
  0.113145      0.386855      0.613145    S
```

(c) An example of POSCAR file

```
[ypochareddy@hpc11:k555]$ grep TITEL POTCAR
   TITEL  = PAW_PBE Mg 13Apr2007
   TITEL  = PAW_PBE Mn_pv 02Aug2007
   TITEL  = PAW_PBE S 06Sep2000
```

(d) An example of POTCAR file

Figure 3.5: Input files

Table 3.1: Tags in the INCAR file

Tag	Description
ENCUT	Specifies the cutoff energy for the planewave basis set. An ENCUT value of 520 eV is chosen. More about the choice is explained in Section 3.3.3
ISTART	Tells the program if it should choose existing wavefunctions data (in the form of WAVECAR file from previous simulation) or to create the orbitals from the scratch. A value of 0 means VASP should create orbitals from scratch. If a value of 1 is given, then the user must also provide WAVECAR file in addition to that of INCAR, KPOINTS, POTCAR, and POSCAR files.
ICHARG	Tells VASP on how to contruct the initial charge density. Similar to ISTART. A value of 2 means VASP takes the superposition of atomic charge densities and a value of 1 means the user must provide VASP with an existing CHGCAR file.
PREC	Specifies the accuracy with which VASP must perform the calculations. 'Accurate ' is the highest possible precision setting.
NSW	Specfies the maximum number of ionic steps before the calculations are stopped. A value of 1000 is provided so that VASP can relax the given structure well. Usually, the program doesn't take more than 100 steps to obtain a relaxed structure.
ISIF	Tells the program which degrees of freedom can be changed during relaxation. A value of 3 means the program is allowed to change the ionic positions, cell volume and cell shape. When a value of 2 is given, the program can only change the ionic positions.
IBRION	Tells the program how the ions can be updated and moved during calculation. For the ionic relaxation, two different IBRION settings can be used i.e. IBRION = 1 and 2. However, as mentioned in the VASP wiki, IBRION value of 1 fails if the initial guess is bad. Hence, an IBRION value of 2 is chosen. For NEB calculation, IBRION value of 3 is given as input.
LREAL	Defines if the projection operators should be evaluated in real or reciprocal space. Here, LREAL is set to Auto, so the projection is done in real space, and the projection operators are fully automatically optimized with no user interference.
ISMEAR	Specifies how the partial occupancies are set for each orbital. VASP wiki suggests the use of tetrahedron method with Blochl corrections for the calculation of total energy of the materials. Hence a value of -5 is used since the material under study is an insulator.

Table 3.1 continued from previous page

Tag	Description
NPAR	Specifies the number of bands to be treated in parallel. A value of 4 is chosen so that the calculations can be run on multiple of 4 cores.
ISYM	Specifies the use of symmetry. ISYM = 0 means the symmetry is turned off. This is done to allow the system to reach local minima [51]
LWAVE	Tells VASP if it needs to write the the wavefunctions to a WAVECAR file for use in subsequent calculations. Here, it is set to false, since we dont use the previous WAVECAR files for next relaxation.
LCHARG	Similar to LWAVE, except charge densities are written to CHGCAR and CHG files.
ISPIN	Tells the program is spin polarization is to be considered for calculations. A value of 2 indicates that spin polarisation must be considered.
MAGMOM	Used to specify the magnetic moments of all atoms in POSCAR file, also according to the order in POSCAR file.
LDAU	LDAU tag specifies if VASP should include effective U values in the calculations.
LDAUL	Tells the program if U values must be considered or not. A value of 2 means LDAUU values must be included in calculations and -1 means LDAUU values should not be included.
LDAUU	Ueff values of each element in the POSCAR, also according to the order in POSCAR file. More about this is discussed in Section 3.3.5.
LDAUJ	LDAUJ tag specifies the strength of the effective onsite exchange interactions. More about this is discussed in Section 3.3.5.
LDAUTYPE	LSDAUTYPE specifies the L(S)DA+U approach to be used. Here, LSDAUTYPE = 2 is chosen because it is a simplified approach by Dudarev et al. [52], compared to others under the same tag.
LMAXMIX	LMAXMIX tag is used to control up to which l-quantum number the one-center PAW charge densities are pass through charge density mixer and written to CHGCAR file. LMAXMIX value of 4 is given because the calculations only involve up to d transition elements.
LASPH	LASPH tag specifies the VASP to include non-spherical contributions related to the gradient of density in the PAW spheres. Here a value of true is used to also include the non-spherical contributions for gradient corrections inside the PAW spheres.
LDAUPRINT	LDAUPRINT tag tells VASP if it should write the occupancy matrix to the OUTCAR file. A value of 1 means VASP will write the occupanyc matrix to OUTCAR file.

3.3. CONVERGENCE TESTS

In this section, the choices made for KPOINTS, INCAR, POTCAR files have been explained. For all convergence tests, $MgMn_2S_4$ spinel has been used (See Figure 3.6). Manganese spinel has been chosen because in this study, it is the only element with U_{eff} values and hence would serve as a good candidate for the comparison of energies when different input values are given to VASP. It must be noted that all the energies reported in this study are per unit cell.

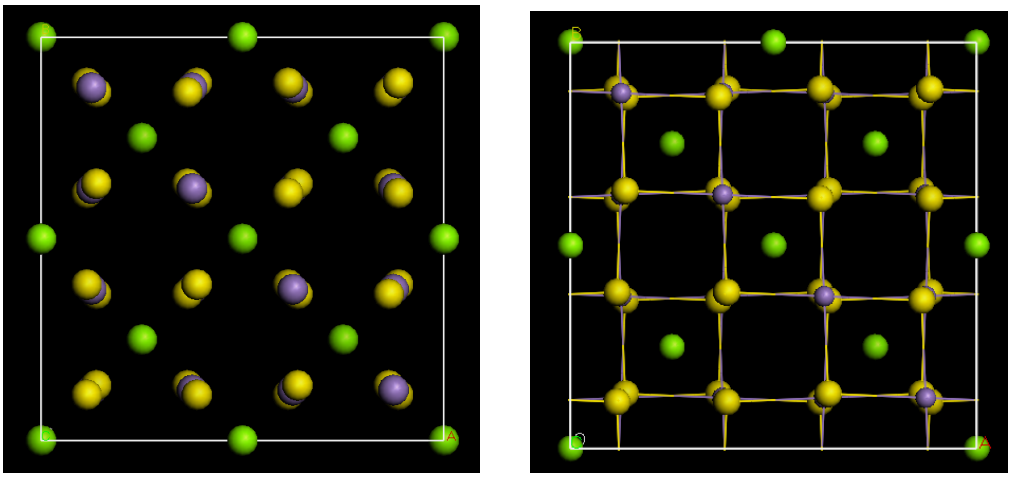

(a) $MgMn_2S_4$ Spinel - before relaxation (b) $MgMn_2S_4$ Spinel - after relaxation

Figure 3.6: MgMn2S4 Spinel

3.3.1. FINDING THE ENERGY PER MAGNESIUM ATOM

The average voltage of the intercalation reaction can be calculated by the following equation [9]:

$$V = \frac{E_{charge} + nE_{Mg} - E_{discharge}}{nz} \tag{3.14}$$

where, n is the number of intercalating atoms, z is the oxidation state of Mg, E_{charge} and $E_{discharge}$ are the calculated energies of the charged and discharged phases, respectively, and E_{Mg} is the energy per Mg atom. E_{charge}, also know as the Energy of the deintercalated phase, is calculated either by deleting the atoms through Materials Studio software or by deleting the information related to Mg atoms in the POSCAR file.

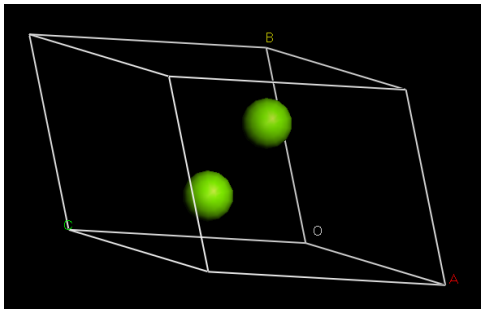

Figure 3.7: Mg metal structure with two Mg atoms

For the given structure in Figure 3.7, the lattice parameters are 3.2094, 3.2094, and 5.2105. Suitable KPOINTS were found by first taking the multiplicative inverse of the lattice parameters, and then multiplying the values with the largest lattice parameter. Since VASP only accepts whole numbers as KPOINTS, the values obtained were multiplied by a whole number and rounded off. The procedure is also illustrated in Figure 3.8. It must also be noted that the multiplication factor can be either odd or even number but an odd number is usually preferred to reduce symmetry related problems during simulation [53]. Hence, an odd number is chosen here.

a	b	c	
3.2094	3.2094	5.2105	Take Inverse
0.3116	0.3116	0.1919	Multiply by 5.2105
1.624	1.624	1.000	Multiply by 3
4.870537	4.870537	3	Round off to nearest whole number
5	5	3	

Figure 3.8: KPOINTS calculation

In order to calculate the voltage, apart from the energy of the host compounds, the energy per Mg atom is required. To do this, a Mg metal structure Figure 3.7 from the Materials studio was taken and relaxed (i.e. DFT calculations are run) with different KPOINTS. The INCAR file used is shown in Figure 3.9 and the VASP suggested pseudopotentials were used.

```
[ypochareddy@hpc11:k553]$ more INCAR
ENCUT = 520
ISTART = 0
ICHARG = 2
PREC = Accurate
NSW = 1000
ISIF = 3
IBRION = 2
LREAL = Auto
ISMEAR = 1
NPAR = 4
ISYM = 0
LWAVE = .FALSE.
LCHARGE = .FALSE.
ISPIN = 2
MAGMOM = 2*0.6 #Mg
```

Figure 3.9: INCAR file used for finding out Energy per Mg atom

Ground-state energies obtained for the structure in Figure 3.7 at different KPOINTS are listed in Table 3.2. In Table 3.2, column 3 is the energy difference (in meV) between the current KPOINTS row and the next one. When the values is Table 3.2 are plotted, Figure 3.10 is obtained. From the Figure 3.10, it can be observed that the energy difference is lowest between 15x15x7 and 17x17x7 KPOINTS. Therefore, the energy corresponding to the KPOINTS 15x15x7 indicated by a black circle around the marker point in Figure 3.10, is the energy of the structure. Since, the structure has two atoms and but the energy required is per Mg atom, the value was divided by 2 to get an energy per Mg atom (E_{Mg} of -1.50809 eV.

Table 3.2: Ground state energies of Mg metal structure for different KPOINTS

KPOINTS	Energy (eV)	Difference in energy (meV)
5x5x3	-3.078399	44.5462
7x7x3	-3.033853	59.4943
9x9x3	-2.974359	32.6219
9x9x5	-3.006980	25.824
11x11x5	-3.032804	21.2563
13x13x5	-3.011548	8.8141
15x15x5	-3.020362	16.3147
13x13x7	-3.004048	12.1491
15x15x7	***-3.016197***	***1.511***
17x17x7	-3.017708	8.473
19x19x9	-3.009235	

3.3.2. CHOOSING KPOINTS FOR THE STUDY

For further DFT calculations of the unit cells, KPOINTS must be chosen. To choose a suitable KPOINTS, convergence tests have been done on $MgMn_2S_4$ structure. Lattice parameters before and after relaxation are tabulated in Table 3.4. From Table 3.4, it can be seen that the lattice parameters a, b and c are equal, therefore the digits in KPOINTS should also be equal. Three tests were carried out with 3x3x3, 5x5x5 and 7x7x7 KPOINTS, keeping INCAR (Figure 3.5a), POSCAR and POTCAR (VASP suggested) files same. Energies of the structures after one relaxation run are presented in Table 3.3, and the energy differences are also calculated and presented in the same table. It can be seen that the energy difference between 3x3x3 and 5x5x5 is 0.26 meV and between 5x5x5 and 7x7x7 is 2.48 meV, and both are below 10 meV. 5x5x5 KPOINTS have been chosen since, they offer a good balance between accuracy and computation time.

Table 3.3: KPOINTS covergence test

KPOINTS	Energy (eV)	Difference in energy (meV)
k333	-301.62776	0.26
k555	-301.62802	2.48
k777	-301.63050	

Table 3.4: Lattice paramters of the MgMn2S4 spinel before and after relaxation

Lattice parameter	MgMn2S4 - before relaxation	MgMn2S4 - after relaxation
a (Å)	10.309	10.478
b (Å)	10.309	10.478
c (Å)	10.309	10.478
alpha (°)	90.00	90.02
beta (°)	90.00	90.02
gamma (°)	90.00	89.99
Volume ($Å^3$)	1095.593	1150.363

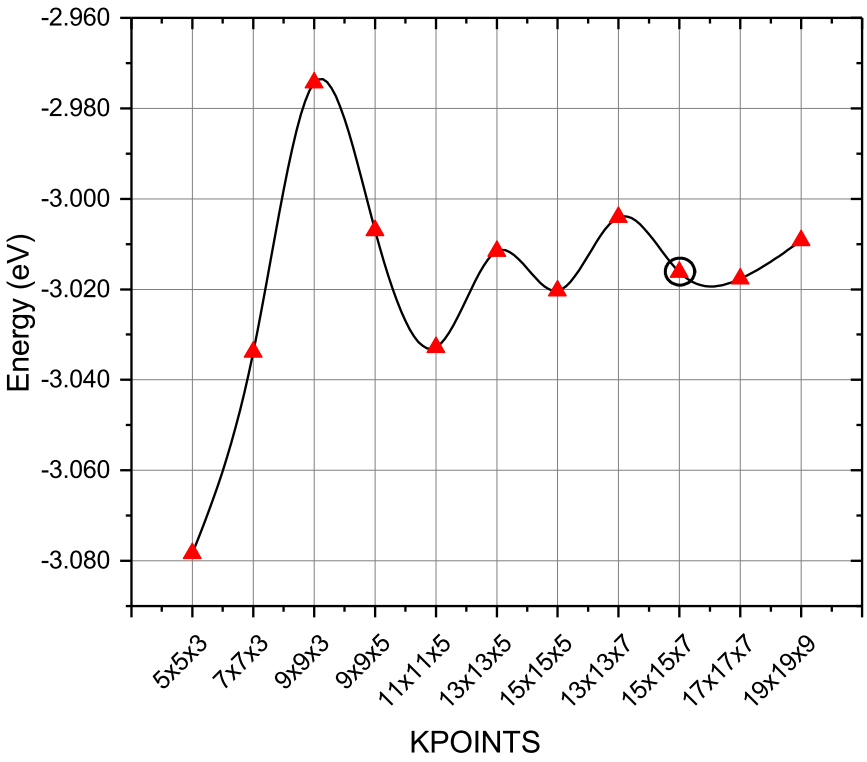

Figure 3.10: Mg metal KPOINTS convergence

3.3.3. EFFECT OF ENCUT ON THE GROUND STATE ENERGY

Usually ENCUT value in the INCAR file is equal to maximum of the ENMAX's in POTCAR files of the elements in the system (ENCUT = max(ENMAX of Mg/Ti_sv/Mn_sv/S)). According to this, ENCUT should be 275 eV (corresponding to Ti_sv POTCAR file). However, for cell shape and volume relaxations i.e. *ISIF* = 3, ENCUT should be increased by 30% [46], which brings the ENCUT value to 357.5 eV. When this value is verified with reference study [9], it is found that they have used 520 eV as their ENCUT. This could be because of two reasons. First reason is that the POTCAR file for Magnesium they [9] have used is Mg_pv and the corresponding ENMAX and ENCUT values are 404 eV and 525.2 eV (520 eV), respectively, and the second reason is that the same authors have also studied oxygen spinels (ENMAX = 400 eV and corresponding ENCUT = 520 eV (1.3*400 eV)) before studying sulfur spinels and therefore would have chose to keep the ENCUT as 520 eV to compare the results of oxygen and sulfur spinels.

Table 3.5: VASP suggested POTCAR files of elements and their ENMAX values.

Name of the POTCAR file	Default cutoff (ENMAX) (eV)
Mg	200
Mn_pv	270
Ti_sv	275
S	259

Therefore, even in this study to be able to compare the results with that of the reference

study [9], ENCUT value is chosen as 520 eV and also an extra calculation with ENCUT as 500 eV was also performed to see check the energy differences. When the ENCUT value is reduced to 500 eV, an energy difference of 10.82 meV (just above 10 meV) was observed (See Table 3.6). This value is closer to the threshold indicating that ENCUT doesn't have much effect on the ground-state energies.

Table 3.6: Effect of ENCUT variation

ENCUT	Energy (eV)	Difference in energy (meV)
500 eV	-301.61720	10.82
520 eV	-301.62802	

3.3.4. EFFECT OF POTCAR'S ON THE GROUND STATE ENERGY

VASP suggested POTCAR files are included in Table 3.5. However, the reference study [9] has used different POTCAR files. In order evaluate the effect of change in the POTCAR files on the ground-state energy of system, DFT calculations are performed by keeping all the input files same except the POTCAR file. Usually there are two types of pseudopotentials. Ultra-soft (USpp) and Projector Augmented Wave (PAWpp). The USpp's are less accurate because the r_c value in USpp is higher than PAWpp, and PAWpp constructs the electron wave function exactly including the nodes in the core electron region.

As one can see in Table 3.7, there are letters after the element's name. The letters pv and sv indicate that the p and s semi-core states are treated as valence states i.e. more electrons are included or in other words the cut-off radius is reduced and therefore the accuracy is increased. This also explains why the reference study [9] has used the pseudopotentials mentioned in Table 3.7. In order to increase the accuracy and to be able to compare with that of the reference study [9], the same psuedopotentials have also been adopted for this study.

Table 3.7: POTCAR files used in Reference study [9]

Element	**Default cutoff (ENMAX) (eV)**
Mg_pv	404
Mn_pv	270
Ti_pv	222
S	259

DFT calculations were performed by keeping all the files same except POTCAR's, where in one calculation VASP suggested pseudopotentials were used and compared against reference study's [9] pseudopotentials. The difference in ground-state energy is mentioned in Table 3.8. The energy difference is higher, however this can be ignored because highly accurate pseudopotentials (Table 3.7) are used for this study.

It must be noted that from this step onwards, the new POTCARs will be used further study, and studies in Sections 3.3.1, 3.3.2, and 3.3.3 have been reevaluated with new POTCARs and the results are similar to the discussions in those same sections. For the readers reference, a Figure 3.11 with all the values obtained is also provided.

Table 3.8: Influence of change in POTCAR's on E0

Description	Energy (eV)	Difference (meV)
VASP suggested	-301.62802	110.07
Ref. study	-301.51795	

KPOINTS Convergence test (with MAGMOM 0.6/5/0.6, ENCUT 520 eV and Updated POTCARs)		
KPOINTS	Energy (eV)	Difference in energy (meV)
k333	-301.51806	0.11
k555	-301.51795	112.55
k777	-301.63050	
ENCUT Change (500 eV) (with MAGMOM 0.6/5/0.6 and Updated POTCARs)		
500 eV	-301.51143	6.52
520 eV	-301.51795	
MAGMOM Change (0/3/0) (with ENCUT 520 eV and Updated POTCARs)		
0 / 3 / 0 (Mg / Mn / S)	-301.51794	0.01
0.6 / 5 / 0.6 (Mg / Mn / S)	-301.51795	

Mg metal			
Total KPOINTS	KPOINTS	Energy (eV)	Difference in energy (meV)
75	5x5x3	-3.076072	43.3034
147	7x7x3	-3.032769	60.4599
243	9x9x3	-2.972309	32.4078
405	9x9x5	-3.004717	25.6515
605	11x11x5	-3.030368	21.0285
845	13x13x5	-3.009340	8.6293
1125	15x15x5	-3.017969	16.1075
1183	13x13x7	-3.001861	12.4048
1575	15x15x7	-3.014266	1.0714
2023	17x17x7	-3.015338	8.3118
3249	19x19x9	-3.007026	

Energy of the structure (with 2 Mg	-3.014266
Energy per Mg atom (eV)	-1.5071331

Figure 3.11: Results with Updated POTCARs

3.3.5. EFFECT OF U ON THE GROUND STATE ENERGY

DFT usually does not consider the strong onsite coulomb interactions. Since, this study involves the use of d block transition elements with localised d electrons, but for localised d electrons, the onsite coulomb interactions are very strong [54]. Hence, in order to account for this, DFT + U theory has to be used. The U part of DFT+U theory is included in calculations through LDAU, LDAUL, LDAUU, and LDAUJ tags in the INCAR file. U values for the current study were taken from [26]. When the U values are not accounted for, the ground-state energy increases i.e. becomes more negative. This can in turn also affect the average voltage values. Change in ground-state energy and average intercalation voltage is shown in Table 3.9.

Table 3.9: Influence of U on ground state energy and voltage.

Description	Energy (eV)	Difference (meV)	Voltage (V)
U = '4' for Mn, and '0' for Mg & S	-301.51795	28376.84	1.743
U = '0' for Mn, Mg & S (K.A. Persson's group) [9]	-329.89479		~1

From Table 3.9 it can be observed that by not including the U value, the average voltage has reduced from 1.743 to 1. This is because change in U value will affect the difference between ground-state energies of charged and discharged phases. In fact, when the voltages were calculated for both cases, it was found that [9] did not use U values in their DFT calculations and the voltage calculate in this study without U value matched with that of [9]. Hence, in this study U values were considered.

3.3.6. EFFECT OF MAGMOM ON THE GROUND STATE ENERGY

In this study, there are atoms with high magnetic moments such as Mn. However, it is relatively difficult to find the correct magnetic moments from literature. One way is usually to set the MAGMOM value to a larger value 1.2 to 1.5 times that of the experimental magnetic moment value and the VASP will automatically correct it back to the right value (See Figure 3.12). However, over the course of the study the correct MAGMOM values were later found from the Materials project website after a detailed search in the internet. DFT calculations were performed with MAGMOM value of 0, 3, 0 for Mg, Mn and S respectively, and 0.6, 5 and 0.6 for Mg, Mn, and S respectively and compared. It is found that there is only 0.01 meV change in ground state energy (See Table 3.10). However, it should also be noted that this is not always the case. More about this is explained in Section **??**.

Table 3.10: Effect of MAGMOM change

Description	Energy (eV)	Difference (meV)
MAGMOM = 0:3:0 (Mg:Mn:S)	-301.51794	0.01
MAGMOM = 0.6:5:0.6 (Mg:Mn:S)	-301.51795	

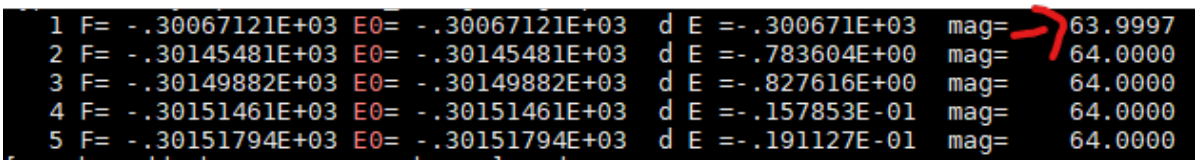

(a) MAGMOM = 0:3:0 (Mg:Mn:S)

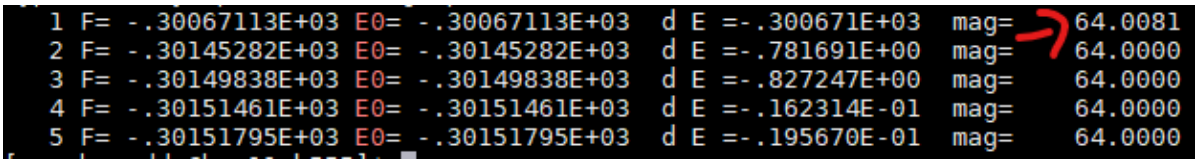

(b) MAGMOM = 0.6:5:0.6 (Mg:Mn:S)

Figure 3.12: VASP MAGMOM correction

It can be noticed from Figure 3.12 that in the first ionic step, the total magnetic moment of structure is 63.997 with MAGMOM = 0:3:0 (Mg:Mn:S), and 64.0081 with MAGMOM = 0.6:5:0.6 (Mg:Mn:S) and the VASP automatically corrects this to the final value of 64 in subsequent ionic steps.

3.4. DOPING

From literature, Mn- and Ti-based sulphur spinels have been identified as a suitable cathode material for Magnesium-ion battery. In this section, the procedure of doping the 'B'part of MgB_2S_4 spinel material i.e. $MgMn_2S_4$ with Ti and vice versa, with another transition metal is described. Initially, a program called 'Cluster 'was used to create doping combinations. Since, the unit cell has 16 octahedral (16c) sites occupied with Mn atoms and each site can be occupied by either Mn/Ti, the program found a total of 2^{16} (65,536) combinations. However, to find the ground-state energies of all 65,536 combinations is possible

but requires huge computation power/time. Since either of those is not available, the author resorted to the use of Manual method i.e. editing the structure in the Materials Studio software. Under each doping combination, 6 configurations with dopant atoms occupying different octahedral sites were made. Each configuration is unique and this was made sure by measuring the interatomic distances in all three directions of the expanded range of unit cell (See Figure 3.14). Doping ratios of 1/16, 2/16, 4/16, 6/16 and 8/16 were chosen (See Figure 3.13). If any of two configurations under a doping ratio combination, have same ground-state energy then one of the configuration is not unique. However, no two configurations were found to have same ground-state energy (See Figure 4.1). Therefore, all the configurations are unique.

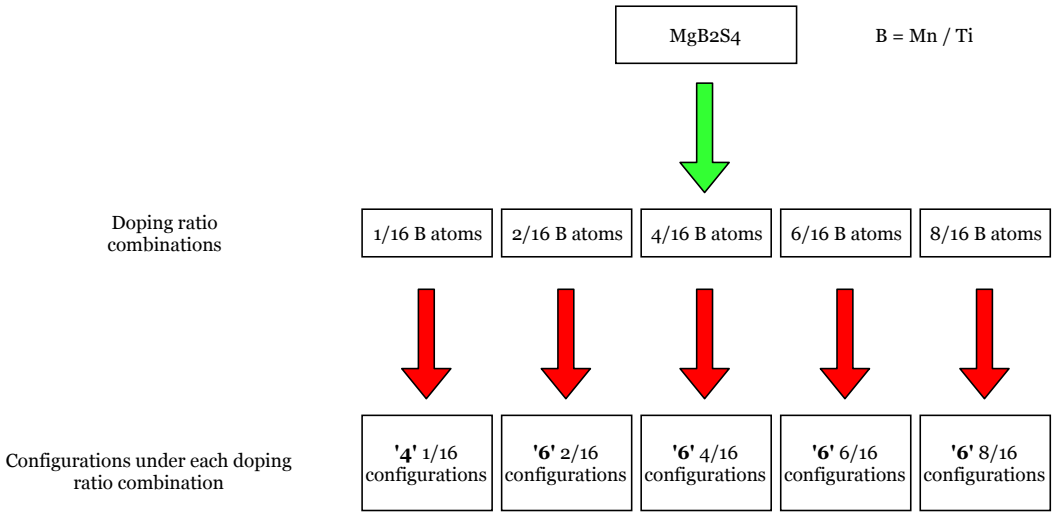

Figure 3.13: An overview of procedure followed to create different configurations under each doping ratio combination

Doping ratio combinations were made in such a way that at the doping ratio of 8/16, the doping of $MgMn_2S_4$ with Ti stops and instead $MgTi_2S_4$ is doped with required amount of Mn to meet exactly at halfway of creating doping combinations. This can be well understood by referring to the Figure 3.15.

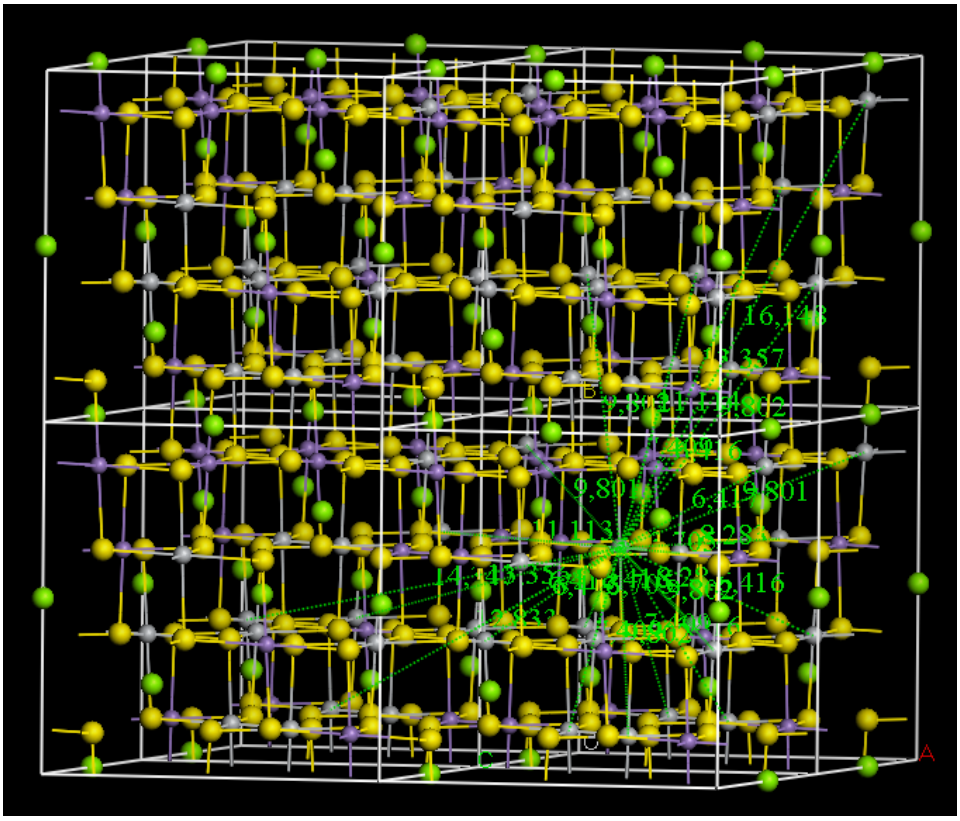

Figure 3.14: An example of an unique 8/16 combination with Interatomic distances drawn

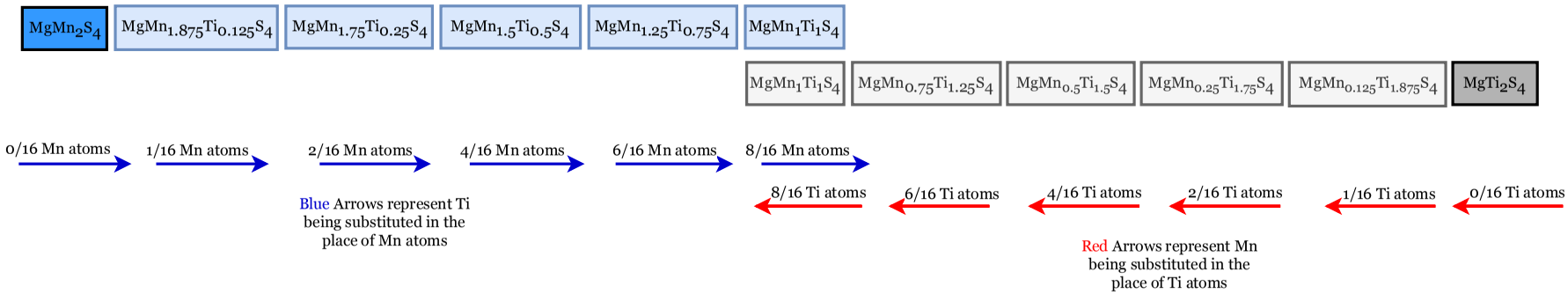

Figure 3.15: A graphical abstract describing the procedure of creating configurations

Once all the configurations were made, they were relaxed twice and then with a one step energy calculation with fixed cell ion positions, cell volume and shape through ISIF = 2 and IBRION = -1 and NSW = 0. Initially, all the configurations' relaxation [3] used POTCAR files suggested by VASP and MAGMOMs of 0 for Mg, S and Ti and 3 for Mn. Resulting ground-state energies were converted to enthalpies of formation in relation with the end members, using Equation 3.15 and Equation 3.16, and plotted as shown in Figure 3.16.

$$H_f = E_{Ti_yHost} - yMgTi_2S_4 - (1-y)MgMn_2S_4 \tag{3.15}$$

$$H_f = E_{Mn_yHost} - yMgMn_2S_4 - (1-y)MgTi_2S_4 \tag{3.16}$$

It can be observed from Figure 3.16, that there are 12 points at x = 1. This is because,

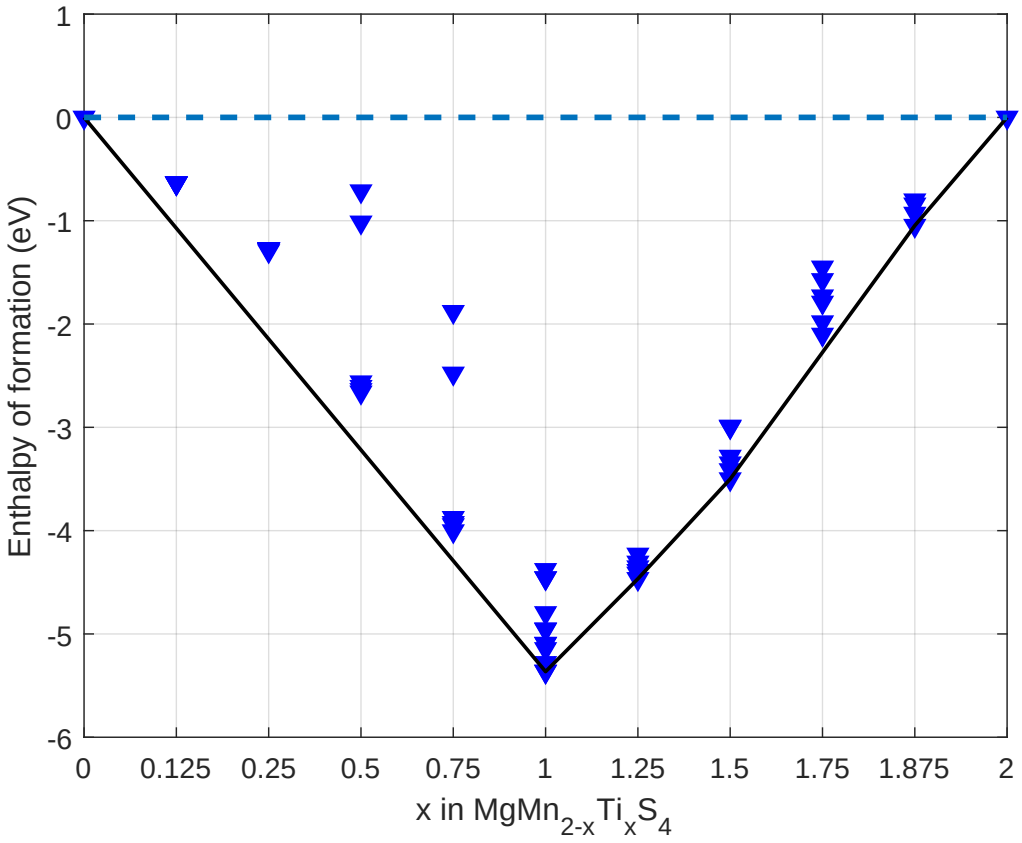

Figure 3.16: Convex Hull with MAGMOM = 0:3:0:0 (Mg:Mn:S:Ti) and VASP suggested POTCARs

as highlighted in Figure 3.15, when doping $MgMn_2S_4$ with Ti at a doping ratio of 8/16, 6 configurations were created, and in addition to that when doping $MgTi_2S_4$ with Mn at a doping ratio of 8/16, 6 more configurations were created. In total, at the doping ratio of 8/16, 12 configurations were obtained and hence the number of points at x = 1 are 12.

Later, the correct MAGMOM's (0.6 for Mg, S and Ti and 5 for Mn) & more accurate POTCAR's were found in Materials Project website, which were also used by [9]. Apart from changing the MAGMOM's and POTCAR's, the second relaxation used the charge densities

[3] Relaxation 2 uses the relaxed atomic positions (CONTCAR file) from relaxation 1.

from the first relaxation. This was done to reduce computation time and is done by changing the LCHARG tag to True in the INCAR file of first relaxation and changing the ICHARG tag to a value of 1 in the INCAR file of second relaxation. The obtained ground-state energies were used to calculate enthalpies of formation, using Equation 3.15 and Equation 3.16, and the results are plotted as shown in Figure 4.1. It can be observed that by comparing Figure 3.16 andFigure 4.1, some combinations have relaxed more after correcting the MAGMOM's and improving the accuracy of pseudopotentials. The relaxed structures were further used for calculating their volume, and this was done by opening the relaxed structure is Material Studio software to find out the lattice parameters.

3.5. NUDGED ELASTIC BAND

To calculate the migration barriers, two methods can be followed: *Ab initio* molecular dynamics (AIMD) and Nudged Elastic Band (NEB). NEB method needs huge computation power/time and AIMD needs even more computation power/time than NEB. To put it in perspective AIMD takes about tens of thousands of steps and each step in AIMD is a DFT calculation [55]. Hence, in this study the focus is to obtain migration barrier for Mg-ion diffusion using NEB method.

It is known that the atoms under a force will follow a minimum energy path under given conditions [6]. Same principle is used in NEB method to identify the migration barriers. In NEB, two states are identified i.e. Initial and Final, which are the same in our case tetrahedral (8a) site. At the inital and final states, the energies are minimal and the forces are zero. This is done by allowing the system to relax by fixing the cell shape volume and volume (ISIF = 2). Following which, using a script (nebmake.pl) developed by Henkelman's group [7], a straight band is drawn between the intial and final state i.e. by creating several equidistant points/images along the straight line path, through extrapolation of atomic positions (See Figure 3.17).

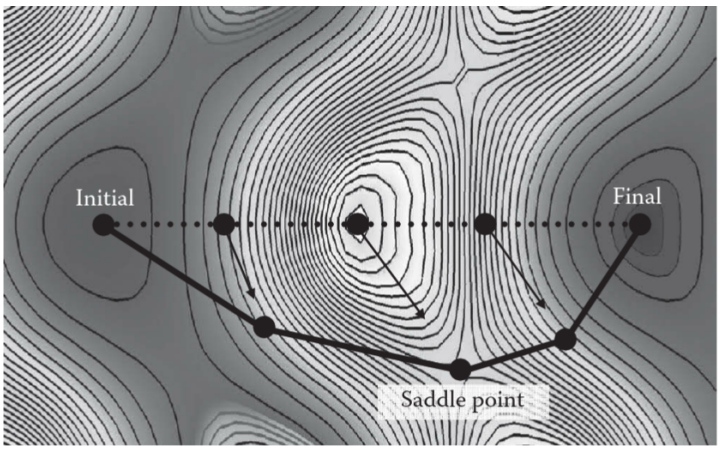

Figure 3.17: Principle of NEB method with three intermediate images, nudging towards the minimum energy path, which passes through the saddle point, where the migration barrier is maximum [6]

The number of points or images are usually 4 - 8, or even more depending on the complexity of the path. Here, in the initial state Mg is in a tetrahedral (8a) site and in the final state Mg is in a nearby tetrahedral (8a) site. Minimum energy path is found by moving (nudging) the bands towards the zero-force configurations [6]. Since NEB method mainly

depends on lowering the forces, IBRION = 3, a damped molecular dynamics algorithm is used for NEB calculation [6]. To make sure that the highest energy image to moves to the saddle point i.e. the point where the energy is the highest, Climbing Image NEB method is adopted for this study (See Figure 3.18). A sample INCAR file for the CI-NEB calculation

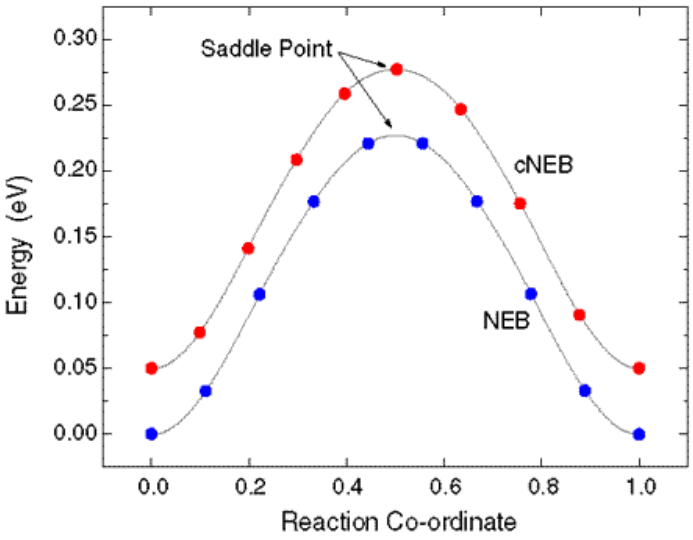

Figure 3.18: Climbing Image NEB vs. NEB [7]

```
ENCUT = 520
ISTART = 0
ICHARG = 2
PREC = Accurate
NSW = 5000
ISIF = 2
IBRION = 3
LREAL = Auto
ISMEAR = -5
NPAR = 4
ISYM = 0
LWAVE = .FALSE.
LCHARG = .FALSE.

SIGMA = 0.2
EDIFF = 1E-5
EDIFFG = -1E-2
POTIM = 0.2
IALGO = 38
LSCALAPACK = .FALSE.

ICHAIN=0
IMAGES=8
SPRING=-5.0
LCLIMB=.TRUE.
LTANGENTOLD=.FALSE.
LDNEB=.FALSE.
LNEBCELL=.FALSE.
```

Figure 3.19: INCAR file of a NEB calculation

is shown in Figure 3.19. Number of images is set through the tag IMAGES, Climbing Image method is enabled by setting LCLIMB as true. As already mentioned, NEB calculations are huge and can take many steps to converge, hence, NSW is set to 5000. Other settings in

INCAR file were according to the suggestions NEB code developers [7]. Detailed procedure and theory of NEB calculations can be found in [43] and [6].

4

RESULTS AND DISCUSSION

In this chapter, the stability (with respect to end members), average intercalation voltage, and volume change of the doped combinations are discussed in the Sections 4.1, 4.2, and 4.4, respectively. Following the discussion of stability and voltage, two doped combinations and the end members are selected for the study of spinel inversion and migration barrier, and the results are discussed in Sections 4.3, and 4.5, respectively. In Section 4.6, the site energy differences of the host structure when Magnesium is octahedral and tetrahedral sites are discussed. Finally, towards the end of the chapter, in Section 4.7, suggestions for further study of the material are provided.

4.1. CONVEX HULL

As explained previously in Section 3.4, at each doping ratio, 6 configurations of $MgMn_2S_4$ spinel doped with Ti, and $MgTi_2S_4$ spinel doped with Mn are created. After finding the ground-state energies of all configurations, the enthalpies of formation (H_f) are calculated using Equation 4.1 and Equation 4.2 [5].

$$H_f = E_{Mn_yHost} - yE_{MgMn_2S_4} - (1-y)E_{MgTi_2S_4} \tag{4.1}$$

$$H_f = E_{Ti_yHost} - yE_{MgTi_2S_4} - (1-y)E_{MgMn_2S_4} \tag{4.2}$$

Where, y is the doping ratio (1/16, 2/16, 4/16, 6/16, and 8/16). The calculated enthalpies of formation are plotted and is shown in Figure 4.1. The endpoints in the graph are the end members $MgMn_2S_4$ (at x = 0) and $MgTi_2S_4$ (at x = 2). If H_f (red inverted triangle in the Figure 4.1) is greater than 0, then the corresponding structure is unstable with respect to the end members. However, this is not the case here. Here, all the red inverted triangles are less than the value of 0, therefore all the configurations tested at all doping ratios are stable with respect to the end members. To plot the convex hull, the end member must be connected with the lowest H_f of all the configurations tested. Here, the lowest point lies at x = 1 i.e. $MgMnTiS_4$. Therefore, a straight line is drawn between the H_f of $MgMn_2S_4$ and the lowest H_f of $MgMnTiS_4$. Therefore, it can be said that the lowest H_f is most stable structure of all the configurations tested, when compared to the end members. In other words, the end members prefer to mix and this will result in the most stable configuration at the point where Mn content is equal to Ti content in the spinel.

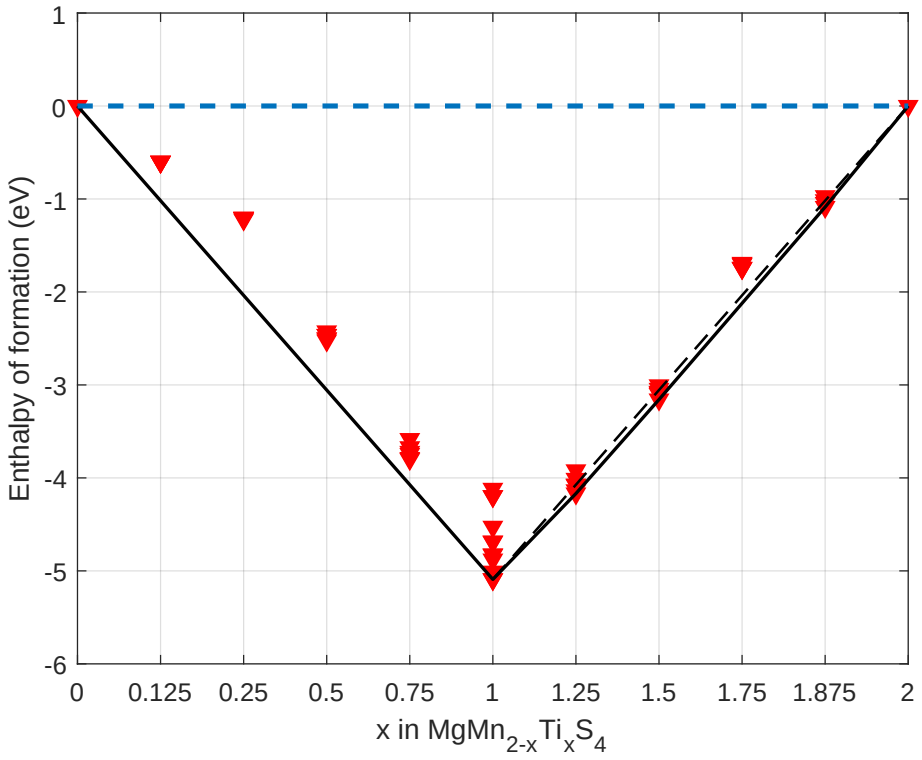

Figure 4.1: Calculated enthalpies of formation at different doping ratios.

Following which, as per the normal procedure, one would think that a straight line should be drawn between the end member $MgTi_2S_4$ and lowest H_f value ($MgMnTiS_4$). However, this is not the case because if a straight line is drawn, there would be some points below the line (See the dashed black line in Figure 4.1).

Any points below the line are considered to be stable and these points ($MgMn_{0.75}Ti_{1.25}S_4$, $MgMn_{0.5}Ti_{1.5}S_4$, and $MgMn_{0.125}Ti_{1.875}S_4$) would become a part of the convex hull. Therefore, the convex hull is the line joining the end member $MgMn_2S_4$, lowest H_f of all the configurations ($MgMnTiS_4$), lowest H_f of $MgMn_{0.75}Ti_{1.25}S_4$, lowest H_f of $MgMn_{0.5}Ti_{1.5}S_4$, lowest H_f of $MgMn_{0.125}Ti_{1.875}S_4$, and the end member $MgTi_2S_4$.Therefore, it can be said that the combinations $MgMnTiS_4$, $MgMn_{0.75}Ti_{1.25}S_4$, $MgMn_{0.5}Ti_{1.5}S_4$, and $MgMn_{0.125}Ti_{1.875}S_4$ are stable. However, for the reasons that will be explained in the next section, only $MgMnTiS_4$, and $MgMn_{0.75}Ti_{1.25}S_4$ will be considered for Spinel inversion, and Migration barriers testing.

It can also be observed that the doping combinations with high Ti content are part of the convex hull. This could be because the $MgTi_2S_4$ structure has a low energy above hull compared to $MgMn_2S_4$ [9]. The term energy above hull (EAH) refers to the driving force of decomposition of the material into its set of most stable materials at that composition. Higher the EAH, lower the thermodynamic stability of the material and vice versa. Figure A.1 illustrates how the EAH of a particular material is calculated.

4.2. AVERAGE INTERCALATION VOLTAGE (VS. MG/MG^{2+})

In this section, average intercalation voltage is used as a criteria for further selection of cathode materials. It must be noted that that all the voltages reported here are against Mg/Mg^{2+}. Average intercalation voltage can be calculated using the Equation 4.3 [9]:

$$V = \frac{E_{charge} + nE_{Mg} - E_{discharge}}{nz} \tag{4.3}$$

Where, E_{charge} is the ground-state energy of charged/deintercalated phase, $E_{discharge}$ is the ground-state energy of discharged/intercalated phase, E_{Mg} is the ground-state energy per Magnesium atom, n is the number of intercalating atoms, and z is the oxidation state of Mg.

As already mentioned in Section 3.2, 8 Mg atoms are intercalated into the structure and oxidation state of Mg is 2. For the calculation of voltage, the most stable configuration at each doping ratio is chosen. Ground-state energy of the charged/deintercalated phase is calculated by removing all the Magnesium atoms from the structure. After obtaining the ground-state energy of deintercalated phase, the values are substituted in Equation 4.3 to find the average intercalation voltage. The calculated average voltages are then plotted as shown in Figure 4.2.

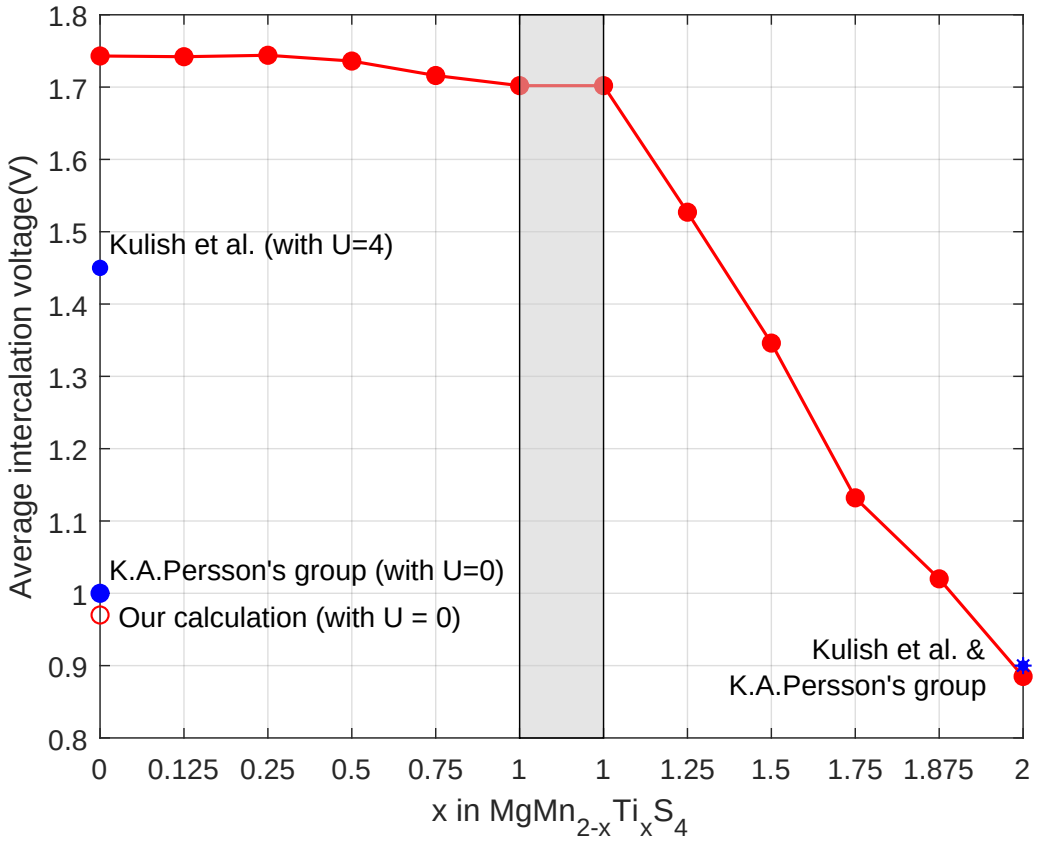

Figure 4.2: Average intercalation voltage vs. Ti content

In Figure 4.2, the greyed out area in the middle represents the average voltage of the $MgMnTiS_4$ combination, where $MgMn_2S_4$ is doped with Ti and $MgTi_2S_4$ doped with Mn at

the same doping ratio of 8/16, to obtain 2 voltage values. Since the values are same (the points at both ends of greyed out part) for the same structure ($MgMnTiS_4$), the calculations are in agreement with each other.

The end members $MgTi_2S_4$ and $MgMn_2S_4$ have voltages 0.885 and 1.743 V, respectively. The average voltage of the end member $MgTi_2S_4$ matches with that of the literature [9] & [26]. However, in the other end member $MgMn_2S_4$, there are some discrepancies. For example, the average voltage calculated by Liu et al. (Mentioned as K.A.Persson's group in the figure) [9] is approximately 1 V. Initially, this caused confusion of whether the calculations done by the author are correct. However, after further investigation, it is found that K.A.Persson's group [9] has calculated the average voltage without considering the U parameter. As explained in Section 3.3.5, the inclusion of the 'U' parameter in the calculation is important to account for the onsite coulomb interactions in Mn sulphur spinel. Therefore, after carrying out calculations by setting U value as 0, an average voltage of 0.97 is obtained, which is approximately equal to the voltage reported by K.A.Persson's group [9]. In addition to that, the average voltage of $MgMn_2S_4$ found in this study did not match with another study (Kulish et al. [26]). However, even after using the same settings as Kulish et al. [26], an average voltage of 1.743 V is was obtained. In addition to that, Kulish et al. [26], in their study mentioned that when Mg is in 16c octahedral sites, an average voltage of 2.01 V was obtained. However, in their plot they have used a different value. This could also mean that there is a discrepancy in the reference [26].

With respect to the voltage trend, the average voltages can be related to the changes in the electronic configuration of charged and discharged states. Ti in the charged phase has an oxidation state of +4, corresponding to d^0, a highly stable configuration. Since Ti exists in a stable oxidation state in charged phase, the average voltage is lower for the end member $MgTi_2S_4$ [26].

In Mn_2S_4 compound, Mn exists in the oxidation state of +4, with stable half-filled t_{2g} states [9]. However, when intercalated with Mg, the extra electrons will change the oxidation state of Mn from 4+ to 3+/2+, leading to high voltages. In the region of $x < 1$, the Ti remains inactive i.e. in its oxidation state of +4. This means the Mn atoms must be dominating the average voltage by gaining electrons and becoming Mn^{2+}/Mn^{3+} and thereby increasing the average voltage. However, beyond $x = 1$, since the Ti content is higher and the Ti atoms become active and gets reduced to Ti^{3+} and the average voltage reduces. However, to better understand the oxidation states of the ions in the structure and the amount of ions in different oxidation states, XRD studies similar to [56] must be conducted.

Since, the combinations $MgMn_{0.5}Ti_{1.5}S_4$, and $MgMn_{0.125}Ti_{1.875}S_4$ offer very low voltages, they are not considered for further study. This leaves $MgMnTiS_4$ and $MgMn_{0.75}Ti_{1.25}S_4$, apart from the end members, for spinel inversion and migration barrier investigations.

It must be noted that the voltage values reported in this section do not represent the actual operating voltages of the battery. More about this is discussed in the Recommendations Section 4.7.

4.3. SPINEL INVERSION

In a normal sulphur spinel, 8 intercalant atoms occupy tetrahedral (8a) sites, and 16 transition metal atoms occupy octahedral (16d) sites. However, in an inverse spinel, the transition metal atoms occupy all the tetrahedral (8a) sites and half of the octahedral (16d) sites, and the intercalant atoms occupy the octahedral (16d) sites [5]. To evaluate if the cathode

candidates $MgMnTiS_4$, and $MgMn_{0.75}Ti_{1.25}S_4$, apart from the end members, are prone to inversion, several inverse configurations are made where the Mn/Ti occupy the tetrahedral (8a) sites at different ratios. The site locations of atoms in the different inverse configurations are listed in Table 4.1. Since the end members are not doped, the configurations are mainly based on placing 8 transition metal atoms in the tetrahedral (8a) sites and placing the intercalant atoms (Mg) in different octahedral (16d) sites.

Table 4.1: Distribution of atoms in tested inverse spinel configurations.

Combination	Configuration	8a (tetrahedral sites)	16d (octahedral sites)
$MgMnTiS_4$ (In Normal spinel, 8 Mg in 8a, 8 Mn in 16d, 8 Ti in 16d)	1	0 Mn 8 Ti	8 Mg 8 Mn
	2	8 Mn 0 Ti	8 Mg 8 Ti
	3	6 Mn 2 Ti	8 Mg 2 Mn 6 Ti
	4	4 Mn 4 Ti	8 Mg 4 Mn 4 Ti
	5	2 Mn 6 Ti	8 Mg 6 Mn 2 Ti
	6	1 Mn 7 Ti	8 Mg 7 Mn 1 Ti
$MgMn_{0.75}Ti_{1.25}S_4$ (In Normal spinel, 8 Mg in 8a, 6 Mn in 16d, 10 Ti in 16d)	1	6 Mn 2 Ti	8 Mg 0 Mn 8 Ti
	2	5 Mn 3 Ti	8 Mg 1 Mn 7 Ti
	3	4 Mn 4 Ti	8 Mg 2 Mn 6 Ti
	4	2 Mn 6 Ti	8 Mg 4 Mn 4 Ti
	5	1 Mn 7 Ti	8 Mg 5 Mn 3 Ti
	6	0 Mn 8 Ti	8 Mg 6 Mn 8 Ti

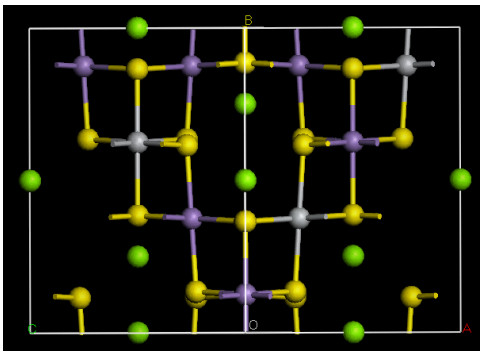

(a) Normal Spinel (Mg in tetrahedral (8a) sites, Ti and Mn in octahedral (16d) sites)

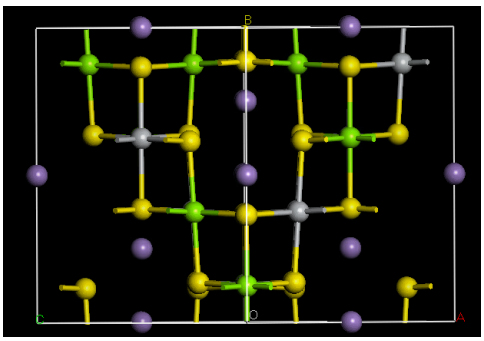

(b) Inverse Spinel (Ti in tetrahedral (8a) sites, Mg and Ti in octahedral (16d) sites)

Figure 4.3: Normal $Mg_{tet}[MnTi]_{oct}S_4$ spinel vs. Inverse ($Mn_{tet}[MgTi]_{oct}S_4$) spinel. Green balls - Mg; Purple balls - Mn; Grey balls - Ti; Yellow balls - S

Figure 4.3 is an example showing the difference between Normal and Inverse spinel configuration of $MgMnTiS_4$. The ground-state energies of the relaxed inverse spinel configurations of different doping combinations are plotted against the ground-state energy of normal spinel (black line with the text preferred) of corresponding doping combination in Figure 4.4. Any point below the preferred line in Figure 4.4 is prone to spinel inversion at high temperatures.

From Figure 4.4 it can be observed that one of the inverse configurations of $MgMnTiS_4$ is prone to spinel inversion and has an energy 738.89 meV lower than its normal spinel.

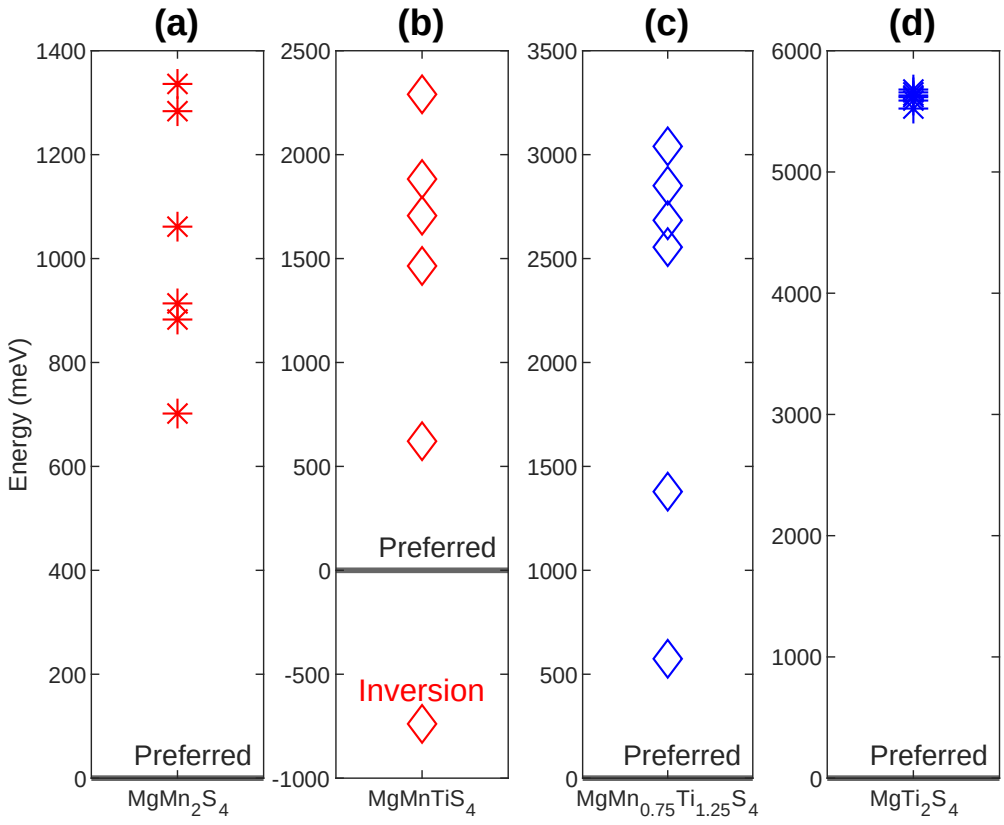

Figure 4.4: Stability of normal spinel vs. inverse spinel for different combinations, where the black line represents preferred normal spinel. (a) Energy of inverse spinel configurations of $MgMn_2S_4$ represented by red asterisks, (b) Energy of the inverse spinel configurations of $MgMnTiS_4$ represented by red diamonds, (c) Energy of inverse spinel configurations of $MgMn_{0.75}Ti_{1.25}S_4$ represented by blue diamonds, and (d) Energy of inverse spinel configurations of $MgMn_2S_4$ represented by blue asterisks.

The inversion prone spinel structure has all the Mn atoms occupying all the tetrahedral (8a) sites. On the other hand, in the combination $MgMn_{0.75}Ti_{1.25}S_4$, the energy of inverse spinel increased with increase in the number of Ti atoms occupying the tetrahedral (8a) sites suggesting that Ti in the structure does not prefer tetrahedral coordination and when forced to sit in tetrahedral (8a) sites will cause instability and increases the ground-state energy of the system. With respect to the end members $MgMn_2S_4$ and $MgTi_2S_4$, no inversion was observed.

Even though the combination $MgMnTiS_4$ shows inversion, it was considered for migration barrier calculations, to get insights in to how the Mn/Ti content influences the migration barriers. Apart from $MgMnTiS_4$, due to positive results obtained for $MgMn_{0.75}Ti_{1.25}S_4$, it was also considered for migration barrier calculations. In total, $MgMn_2S_4$, $MgTi_2S_4$, $MgMn_{0.75}Ti_{1.25}S_4$, and $MgMnTiS_4$ will be evaluated for Mg^{2+} migration barriers.

4.4. VOLUME CHANGE

In this section, the change in the volume of the structure after intercalation, with respect to Ti content is discussed. Figure 4.5 illustrates the change in volume on the left y-axis

and lattice parameter of the intercalated phase on the right y-axis. The volume change

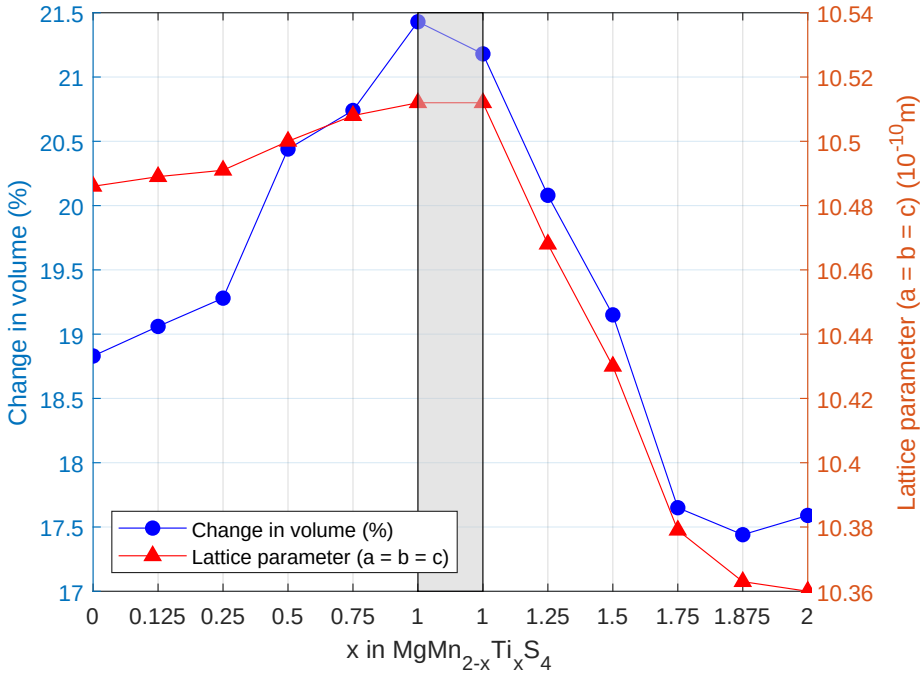

Figure 4.5: Change in volume

observed for the end members $MgMn_2S_4$ (18.83 %) and $MgTi_2S_4$ (17.59 %) is consistent with the literature (18.5 % for $MgMn_2S_4$, and 17.59 % for $MgTi_2S_4$ [26]).

It is observed that the lattice parameter and the volume change increases with Ti content until x = 1, and then decreases. This can be explained with reference to studies conducted on $LiMn_{2-y}Ti_yO_4$ by Yoo et al. [56]. Yoo et al. [56] in their study observed that the lattice parameter increased with increase in Ti content. This increase was attributed to the difference in the ionic radii of octahedrally coordinated Mn^{4+} (0.53 Å) and octahedrally coordinated Ti^{4+} (0.61 Å).

Now going back to the discussion from Section 4.3, it was discussed that the structure ($MgMnTiS_4$) with all Mn atoms occupying tetrahedral (8a) sites is prone to spinel inversion. Therefore, one can say that Mn prefers tetrahedral coordination, and the lattice parameter associated with the inverse spinel is 10.489 Å. When Mn occupies a site that it doesn't prefer i.e. octahedral site instead of its preferred tetrahedral site, the structure tries to accomodate all the atoms by increasing the volume. This is what seems to have led an increase in the lattice parameter (10.512 Å) and high volume change in the $MgMnTiS_4$. On comparing the inverse spinel's (10.489) and the normal spinel's lattice parameters (10.512), one can say that the structures with high Mn content along with Ti doping are prone to inversion. This is also confirmed by testing another combination i.e. $MgMn_{1.25}Ti_{0.75}S_4$ for spinel inversion, where 8/10 Mn atoms from octahedral (16c) sites occupy the tetrahedral (8a) sites.

Table 4.2: Ionic radius of Mn and Ti at different oxidation states [10]

Coordination	Description	Ionic radius (Å)
6	Mn^{2+}	0.83
4	Mn^{2+}	0.66
6	Mn^{3+}	0.645
6	Mn^{4+}	0.53
4	Mn^{4+}	0.69
6	Ti^{4+}	0.61

Beyond x = 1, the reduction in lattice parameter could be because of replacement of octahedrally coordinated Mn^{2+} (ionic radii = 0.83 nm)/tetrahedrally coordinated Mn^{2+} (ionic radii = 0.66 nm)/octahedrally coordinated Mn^{3+} (ionic radius = 0.645 nm) with octahedrally coordinated Ti^{4+} ions i.e. replacement of Mn ions with higher ionic radius than Ti^{4+}.

4.5. MIGRATION BARRIERS

In this section, migration barrier for Mg^{2+} ions in Ti_2S_4 structure at concentrated vacancy limit [1] is discussed. Migration barriers for other structures i.e. Mn_2S_4, $MnTiS_4$, and $Mn_{0.75}Ti_{1.25}S_4$ are not discussed in this report because the calculations are either still running/convergence issues with the structures.

Migration barrier for Mg^{2+} ion along the minimum energy path in Ti_2S_4 structure is shown in Figure 4.6. The dip in the curve at about 50 % of the diffusion path means that

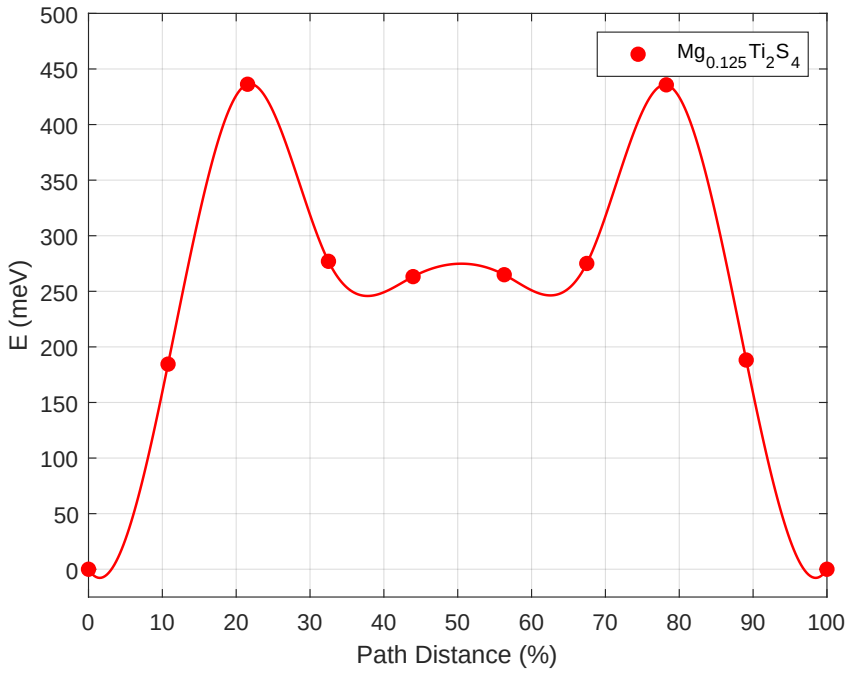

Figure 4.6: Mg-ion migration path between two tetrahedral (8a) sites through an octahedral (16c) site.

the cation moves through a metastable 16c octahedral site. The migration barrier found for

[1] Only one Mg atom is present in the unit cell i.e. $Mg_{0.125}Ti_2S_4$

Mg^{2+} diffusion in Ti_2S_4 structure in this study i.e. 436 meV, is lower than the values reported by Kulish et al. [26], Liu et al. [9], and Emly and van der Ven [24]. This is because in [26], [9], and [24], the migration path is from one octahedral (16c) site to another octahedral (16c) site through a tetrahedral (8a) site. Mg prefers octahedral coordination but placing Mg in a tetrahedral site (a metastable site) will result in a thermodynamically metastable structure which will reduce the migration barrier [32]. Hence, the lower migration barriers in this study compared to the literature. The migration barrier for Mg^{2+} in Ti_2S_4 structure is also less than that of migration barrier needed (525 meV) [32] for adequate operation of battery.

4.6. MG IN OCTAHEDRAL SITES

In the study conducted by Bruce et al. [23], they found that Mg occupied octahedral (16c) sites in the Ti_2S_4 spinel structure. Same was also observed by Sun et al. [25]. Sun et al. [25] on conducting a DFT study to find the site preference of Mg in Ti_2S_4 spinel, they concluded that the spinel with Mg in octahedral (16c) sites is energetically favourable but the energy difference/site energy difference of the spinel with Mg in octahedral (16c) sites and Mg in tetrahedral (8a) sites is small. This was later confirmed by Liu et al. [9]. In addition to that Liu et al. [9] also found that the site energy difference is also small in $MgMn_2S_4$. However, in the two DFT studies on site energy differences, the information about the number of configurations tested is not clearly provided. Therefore, in this study, 16 different configurations where Mg is in different octahedral sites, both in Ti_2S_4 and Mn_2S_4 spinel hosts are tested and compared.

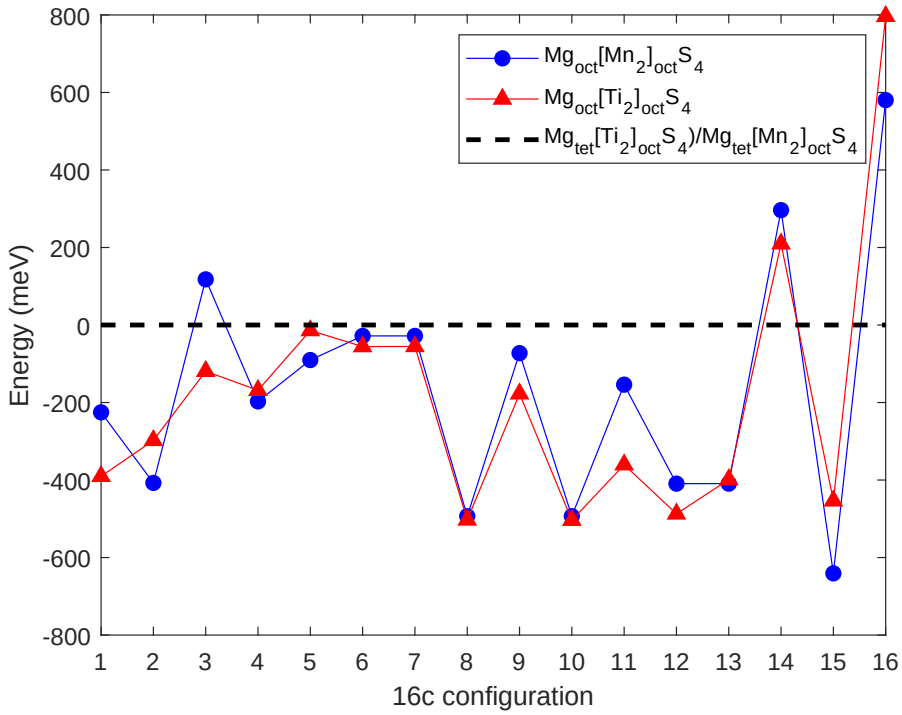

Figure 4.7: Blue line represents the site energy difference between $Mg_{oct}[Ti_2]_{oct}S_4$ and $Mg_{tet}[Ti_2]_{oct}S_4$ (black line), and red line represents the site energy difference between $Mg_{oct}[Mn_2]_{oct}S_4$ and $Mg_{tet}[Mn_2]_{oct}S_4$ (black line) for different configuration of Mg in octahedral (16c) sites.

Figure 4.7 illustrates the site energy difference of Mg in 16 different octahedral site configurations in both Ti_2S_4 and Mn_2S_4 spinel hosts against the Mg in tetrahedral (8a) sites of Ti_2S_4 and Mn_2S_4 spinel hosts.

The dashed black line represents the energy of the corresponding host material with Mg in tetrahedral (8a) sites, and the blue line represents the site energy difference between the Mn_2S_4 struture with Mg in octahedral (16c) sites and Mn_2S_4 structure with Mg in tetrahedral (8a) site. Similarly, the red line also represents the same but in Ti_2S_4 host structure. Any point below the dashed black line corresponds to a stable $Mg_{oct}[B_2]_{oct}S_4$ configuration, where B = Mn/Ti.

Liu et al. [9] reported a site energy difference of approximately 100 meV for both $MgMn_2S_4$ and $MgTi_2S_4$. However, in the current study, a maximum site energy difference of 797 and 641 meV is observed for $Mg_{oct}[Mn_2]_{oct}S_4$ and $Mg_{oct}[Ti_2]_{oct}S_4$, respectively. The difference could be because Liu et al. [9] might not have tested enough configurations or the configuration they have tested could have been something similar to 3rd 16c configuration in the Figure 4.7.

4.7. RECOMMENDATIONS

In Section 4.6, it is discussed that the site energy difference found from this study is higher than the literature. Therefore, the most stable 16c configuration's Mg positions must replace the Mg positions of this study and the stability, average voltage, volume change, spinel inversion and migration barriers must be studied. The author has already setup up all the calculations and they are running at the time of the writing of this report (See Figure A.3).

Following which, the stable combinations from this study ($Mg_{tet}[MnTi]_{oct}S_4$ and $Mg_{tet}[Mn_{0.75}Ti_{1.25}]_{oct}S_4$) must be evaluated against the stable $Mg_{oct}[MnTi]_{oct}S_4$ and $Mg_{oct}[Mn_{0.75}Ti_{1.25}]_{oct}S_4$ configurations, and if the structure with Mg in tetrahedral (8a) sites is stable than the one with Mg in octahedral (16c) sites, then one expect a lower migration barriers in the $Mg_{tet}[MnTi]_{oct}S_4$ and $Mg_{tet}[Mn_{0.75}Ti_{1.25}]_{oct}S_4$ materials than $Mg_{oct}[MnTi]_{oct}S_4$ and $Mg_{oct}[Mn_{0.75}Ti_{1.25}]_{oct}S_4$.

Once the above-mentioned evaluation is done, one can vary the Mg content of structure (for instance, $Mg_xMn_{1.5}Ti_{0.5}S_4$ where x = 0 to 1) to get the average voltages at different states of charge/discharge. This method can be used to give an overview of the voltage profile that one can expect from an actual battery and is a good representation of actual operating voltage of the cell. This method was also proven by Sun et al. [25] in their study on $Mg_xTi_2S_4$, where x is varied from 0 to 1.

One can also try to improve the voltages by substituting Mn/Ti in the structure with V/Fe. However, it must be noted that Liu et al. [9] in their study found that V and Fe sulphur-based spinel materials have a high Energies Above Hull (EAH) compared to Mn and Ti sulphur-based spinel materials. The author has tried doping $MgMnTiS_4$ by replacing the 2 Mn atoms with Fe and V, and it is found that Fe doping has made the structure unstable, whereas V doping has increased the stability of the structure. From the preliminary calculations i.e. not yet converged inverse spinel calculations at the time of writing of this report, it is observed that there is a high possibility that the Vanadium doping in place Mn could work in eliminating spinel inversion. It was also observed that the change in average voltage by V doping is negligible, and volume change also reduced. Although, V doping proves to be useful, it must be noted that V is not a preferred material because of its

toxicity, mining and extraction conditions.

In addition to this, author has also tried intercalating Na into Mn_2S_4 structure. An average intercalation voltage of 1.95 V (vs. Na/Na^+), and a volume change of 25% was observed.

To verify the results from DFT and as an experiment on the actual material, the stable combinations from this study and the subsequent studies, must be synthesized and tested and compared against the DFT calculations. Studies such as Galvanostatic Intermittent Titration Technique (GITT) can also provide experimental verification for migration barriers against DFT calculated migration barrier values. However, before this, the synthesis of $MgMn_2S_4$ spinel material must be carrier out first because, to the best of author's knowledge, no one has reported any synthesis of this material. Doing so would give first-hand insights into the material and would also confirm the DFT calculations.

5

CONCLUSIONS

Initially, this study started off with a goal to only find out the migration barriers of Mg^{2+} moving from tetrahedral (8a) site to the next tetrahedral (8a) site through a transition octahedral (16c) site, in Ti/Cr/V/Fe/Co/Co/Ni doped $MgMn_2S_4$ spinel material, for the use as a cathode in Magnesium-ion battery. However, later the research question expanded into studying the stability, average intercalation voltages, and volume change of doping combinations. After a thorough literature review, $MgMn_2S_4$ and $MgTi_2S_4$ were identified to be stable structures in charge & discharged phases. Therefore, several doping combinations of $MgMn_2S_4$ spinel doped with Ti are made and evaluated. Conclusions of this study are listed as follows:

- With respect to stability, it was found that the doped combinations with high Ti content are more stable than the structures with high Mn content, and therefore these structures became a part of the convex hull. This could be because of low Energy Above Hull (EAH) of $MgTi_2S_4$ as observed by Liu et al. [9].
- With respect to average intercalation voltages (vs. Mg/Mg^{2+}), it was found that with increase in Ti doping content in $MgMn_2S_4$ until the point where Ti content is equal to Mn content, the average voltage was similar to the end member $MgMn_2S_4$ and once the Ti content exceeded Mn content, the average voltage started reducing in a linear fashion. This could be because at low Ti contents, the Ti ion is inactive and exists in its stable 4+ oxidation state. Average voltages of $MgMnTiS_4$, $MgMn_{0.75}Ti_{1.25}S_4$, $MgMn_{0.5}Ti_{1.5}S_4$, and $MgMn_{0.125}Ti_{1.875}S_4$ were 1.702, 1.527, 1.346, and 1.02 V respectively. Since $MgMn_{0.5}Ti_{1.5}S_4$, and $MgMn_{0.125}Ti_{1.875}S_4$ offered very low voltages, they were not considered for spinel inversion and migration barrier studies.
- When spinel inversion tests were conducted on the following four structures: $MgMn_2S_4$, $MgMnTiS_4$, $MgMn_{0.75}Ti_{1.25}S_4$, and $MgTi_2S_4$, spinel inversion was found in $MgMnTiS_4$. The inverse spinel structure was found to be stable than normal spinel structure by ~740 meV.
- On testing to see change in volume of the host structure after intercalation, it was found that the volume change was maximum in doping combination where the Ti content is equal to Mn content, with a trend of increasing volume change until Ti content is equal to Mn content, and decreases from thereon, with further increase

in Ti until Ti completely replaces Mn. This was attributed to Mn ion's tetrahedral coordination preference in combinations with high Mn content than Ti content, but not in the end member $MgMn_2S_4$.

- In the migration barrier studies, only the migration barrier of Mg in Ti_2S_4 structure was found. This was due to severe convergence problems observed/the simulations are still running at the time of report writing, in the other structures. The migration barrier of Mg in Ti_2S_4 was found to be ~ 436 meV. This value is lower than the migration barrier value (525 meV [32]) needed for adequate operation of battery.

Overall, the cathode materials based on sulphur spinel look interesting even though they offer low voltages compared to oxide based spinel cathode materials. However, as suggested in Appendix A, the material $MgMn_{1.5}Ti_{0.5}S_4$ could be a suitable cathode material owing to its high voltage value of 1.770 (vs. Mg/Mg^{2+}), a volume change of only 15%, which is lower that both the end members and all the combinations tested!

A

APPENDIX

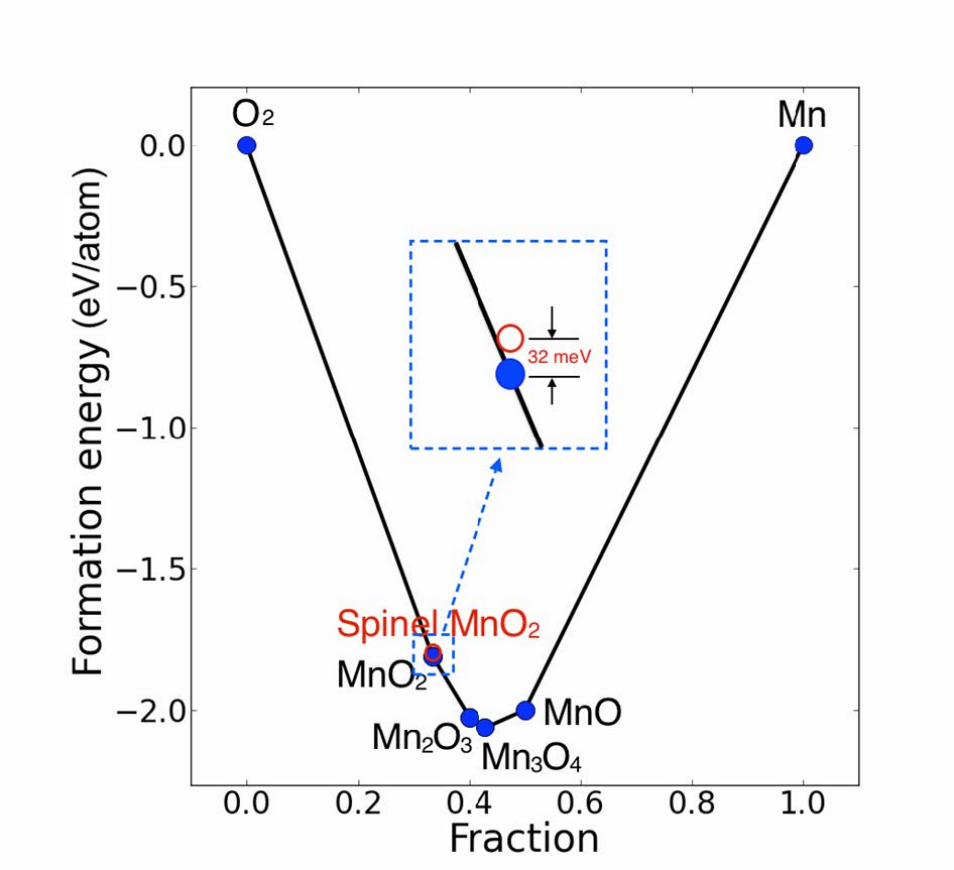

Figure A.1: In Mn-O phase diagram, the lowest formation energy compounds (solid blue dots) i.e. the compounds that cannot be decomposed, are connected to plot a convex hull (black line). Following which, the spinel Mn_2O_4 at a composition similar to MnO_2 is added in the plot as a open red circle. The difference between the formation energy of Mn_2O_4 spinel and MnO_2 is the Energy above Hull (EAH) (ESI of [8]).

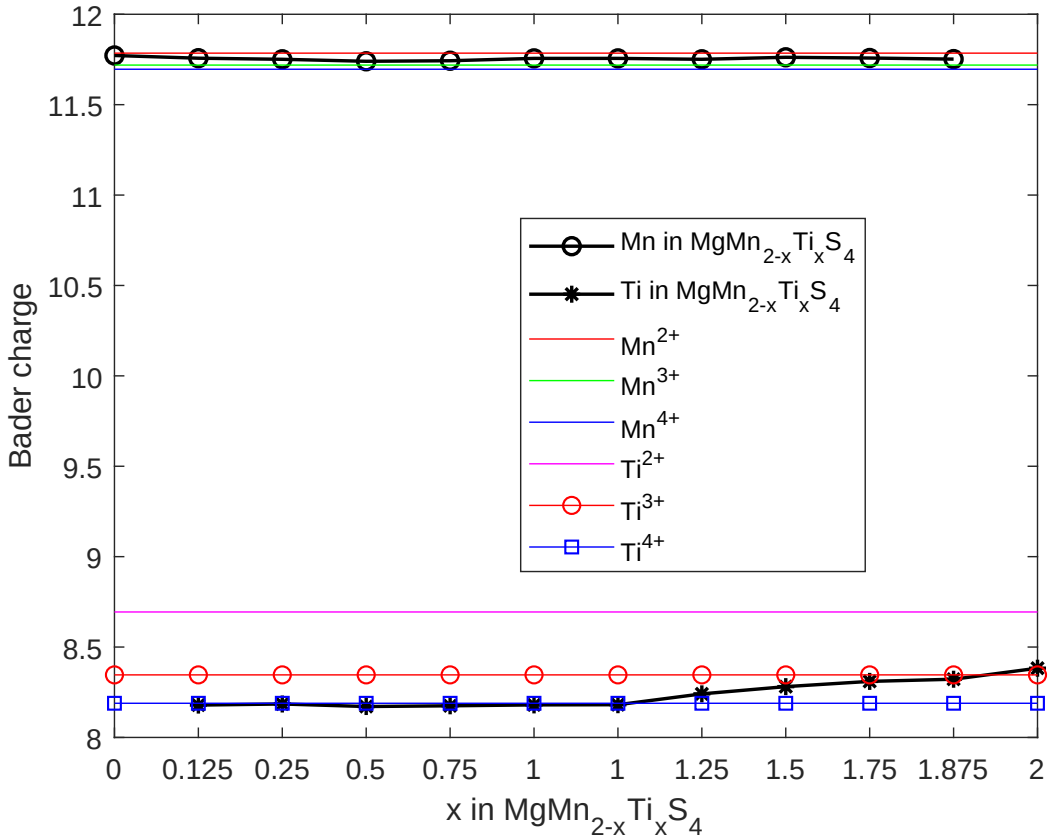

Figure A.2: Average bader charges of Mn and Ti ions in the doping combinations with Mg in tetrahedral (8a) sites. This figure indicates that the Ti is inactive and remains in its stable 4+ oxidation state when Mn content is higher that Ti, and once the Ti content exceeds Mn content, the Ti becomes active and dictates the voltage trend.

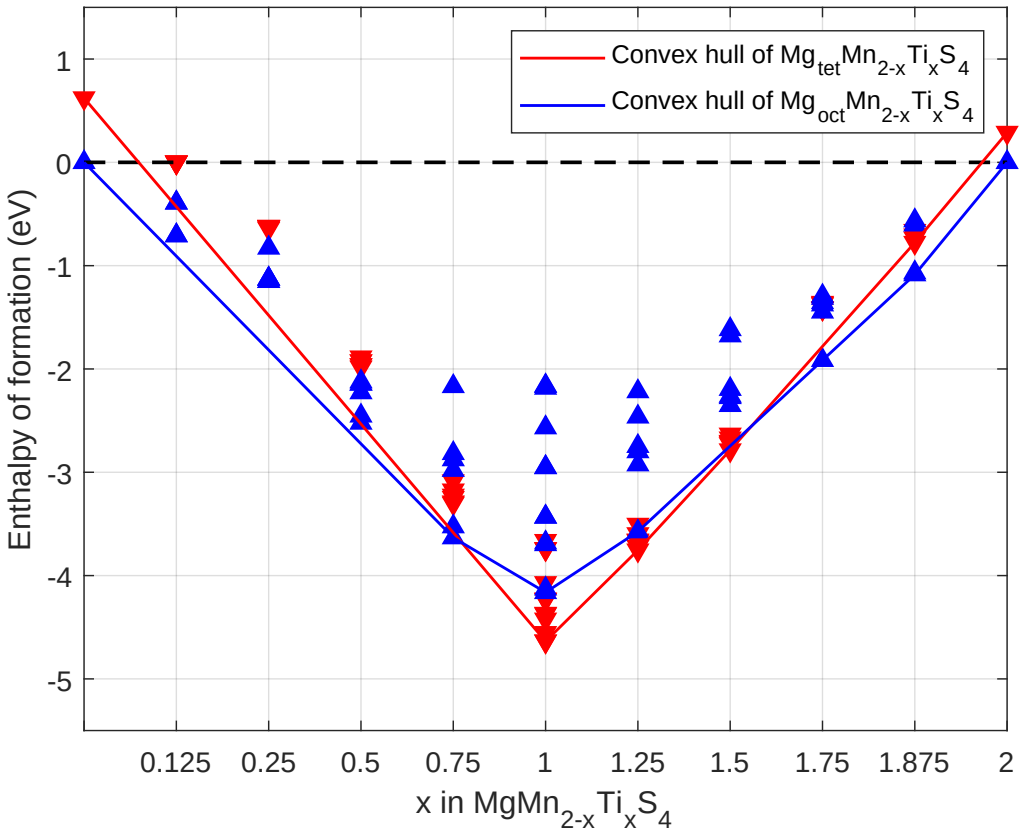

Figure A.3: Blue line represents the convex hull of doping combinations with Mg in the octahedral (16c) sites and red line represents the convex hull of doping combinations with Mg in tetrahedral (8a) sites. It must noted that, from preliminary calculations, the blue point that it part of convex hull i.e. the one corresponding to $MgMn_{0.75}Ti_{1.25}S_4$, may not be suitable because the energy difference between normal and inverse spinel is just 50 meV, and therefore is not suggested for further experimental investigation. However, on the other hand, $MgMn_{1.5}Ti_{0.5}S_4$ could be a suitable cathode material for further experimental studies.

BIBLIOGRAPHY

[1] C. Ling and K. Suto, "Thermodynamic origin of irreversible magnesium trapping in chevrel phase mo6s8: Importance of magnesium and vacancy ordering," *Chemistry of Materials*, vol. 29, no. 8, pp. 3731–3739, 2017.

[2] M. M. Huie, D. C. Bock, E. S. Takeuchi, A. C. Marschilok, and K. J. Takeuchi, "Cathode materials for magnesium and magnesium-ion based batteries," *Coordination Chemistry Reviews*, vol. 287, pp. 15–27, 2015.

[3] G. S. Gautam, P. Canepa, R. Malik, M. Liu, K. Persson, and G. Ceder, "First-principles evaluation of multi-valent cation insertion into orthorhombic v2o5," *Chemical Communications*, vol. 51, no. 71, pp. 13 619–13 622, 2015.

[4] C. Ling, D. Banerjee, W. Song, M. Zhang, and M. Matsui, "First-principles study of the magnesiation of olivines: redox reaction mechanism, electrochemical and thermodynamic properties," *Journal of Materials Chemistry*, vol. 22, no. 27, p. 13517, 2012.

[5] A. Vasileiadis, *Modeling Electrode Materials*. Delft University of Technology, 2018. [Online]. Available: https://repository.tudelft.nl/islandora/object/uuid:3a0da462-b912-4a60-9ff3-6f66b2cd0884

[6] J. G. Lee, *Computational materials science*. CRC Press, Taylor Francis Group, 2017.

[7] [Online]. Available: http://theory.cm.utexas.edu/vtsttools/neb.html#neb

[8] M. Liu, Z. Rong, R. Malik, P. Canepa, A. Jain, G. Ceder, and K. A. Persson, "Spinel compounds as multivalent battery cathodes: a systematic evaluation based on ab initio calculations," *Energy Environmental Science*, vol. 8, no. 3, pp. 964–974, 2015.

[9] M. Liu, A. Jain, Z. Rong, X. Qu, P. Canepa, R. Malik, G. Ceder, and K. A. Persson, "Evaluation of sulfur spinel compounds for multivalent battery cathode applications," *Energy Environmental Science*, vol. 9, no. 10, pp. 3201–3209, 2016.

[10] K. Petrov, R. M. Rojas, P. J. Alonso, J. M. Amarilla, M. G. Lazarraga, and J. M. Rojo, "Cation distribution and phase transformations in limn2ytiyo4 solid solutions," *Solid State Sciences*, vol. 7, no. 3, pp. 277–286, 2005.

[11] IRENA, *Renewable Power Generation Costs in 2017*, 2018. [Online]. Available: https://www.irena.org/publications/2018/Jan/Renewable-power-generation-costs-in-2017

[12] F. Ausfelder, C. Beilmann, M. Bertau, S. Bräuninger, A. Heinzel, R. Hoer, W. Koch, F. Mahlendorf, A. Metzelthin, and M. e. a. Peuckert, "Energy storage as part of a secure energy supply," *ChemBioEng Reviews*, vol. 4, no. 3, pp. 144–210, 2017.

[13] G. De Clercq, "Saudi arabia hopes to export solar electricity to europe," *Reuters*, 2013. [Online]. Available: https://www.reuters.com/article/saudi-solar-europe/saudi-arabia-hopes-to-export-solar-electricity-to-europe-idUSL5N0CY2SX20130411

[14] IPCC, "Climate change 2014: Mitigation of climate change." 2014. [Online]. Available: https://www.ipcc.ch/site/assets/uploads/2018/02/ipcc_wg3_ar5_full.pdf

[15] Gaia, "When will we advance to a Type I civilization on the Kardashev scale?" 2017. [Online]. Available: https://www.gaia.com/article/type-one-kardashev-scale

[16] Z. Ma, D. R. MacFarlane, and M. Kar, "Mg cathode materials and electrolytes for rechargeable mg batteries: A review," *Batteries Supercaps*, vol. 2, no. 2, pp. 115–127, 2019.

[17] Z. Zhao-Karger and M. Fichtner, "Beyond intercalation chemistry for rechargeable mg batteries: A short review and perspective," *Front Chem*, vol. 6, p. 656, 2018. [Online]. Available: https://www.ncbi.nlm.nih.gov/pubmed/30697538

[18] M. Mao, T. Gao, S. Hou, and C. Wang, "A critical review of cathodes for rechargeable mg batteries," *Chem Soc Rev*, vol. 47, no. 23, pp. 8804–8841, 2018. [Online]. Available: https://www.ncbi.nlm.nih.gov/pubmed/30339171

[19] M.-S. Park, J.-G. Kim, Y.-J. Kim, N.-S. Choi, and J.-S. Kim, "Recent advances in rechargeable magnesium battery technology: A review of the field's current status and prospects," *Israel Journal of Chemistry*, vol. 55, no. 5, pp. 570–585, 2015.

[20] C. Kuang, W. Zeng, and Y. Li, "A review of electrode for rechargeable magnesium ion batteries," *J Nanosci Nanotechnol*, vol. 19, no. 1, pp. 12–25, 2019. [Online]. Available: https://www.ncbi.nlm.nih.gov/pubmed/30326998

[21] D. Aurbach, Z. Lu, A. Schechter, Y. Gofer, H. Gizbar, R. Turgeman, Y. Cohen, M. Moshkovich, and E. Levi, "Prototype systems for rechargeable magnesium batteries," *Nature*, vol. 407, no. 6805, pp. 724–727, 2000.

[22] P. G. Bruce, F. Krok, J. Nowinski, V. C. Gibson, and K. Tavakkoli, "Chemical intercalation of magnesium into solid hosts," *Journal of Materials Chemistry*, vol. 1, no. 4, p. 705, 1991.

[23] P. Lightfoot, F. Krok, J. L. Nowinski, and P. G. Bruce, "Structure of the cubic intercalate mg x tis2," *Journal of Materials Chemistry*, vol. 2, no. 1, p. 139, 1992.

[24] A. Emly and A. Van der Ven, "Mg intercalation in layered and spinel host crystal structures for mg batteries," *Inorg Chem*, vol. 54, no. 9, pp. 4394–402, 2015. [Online]. Available: https://www.ncbi.nlm.nih.gov/pubmed/25905428

[25] X. Sun, P. Bonnick, V. Duffort, M. Liu, Z. Rong, K. A. Persson, G. Ceder, and L. F. Nazar, "A high capacity thiospinel cathode for mg batteries," *Energy Environmental Science*, vol. 9, no. 7, pp. 2273–2277, 2016.

[26] V. V. Kulish, D. Koch, and S. Manzhos, "Aluminium and magnesium insertion in sulfur-based spinels: a first-principles study," *Phys Chem Chem Phys*, vol. 19, no. 8, pp. 6076–6081, 2017. [Online]. Available: https://www.ncbi.nlm.nih.gov/pubmed/28191557

[27] X.-L. Li and Y.-D. Li, "Mos2nanostructures: Synthesis and electrochemical mg2+intercalation," *The Journal of Physical Chemistry B*, vol. 108, no. 37, pp. 13 893–13 900, 2004.

[28] Y. Liu, L. Jiao, Q. Wu, J. Du, Y. Zhao, Y. Si, Y. Wang, and H. Yuan, "Sandwich-structured graphene-like mos2/c microspheres for rechargeable mg batteries," *Journal of Materials Chemistry A*, vol. 1, no. 19, p. 5822, 2013.

[29] Y. Liang, R. Feng, S. Yang, H. Ma, J. Liang, and J. Chen, "Rechargeable mg batteries with graphene-like mos2 cathode and ultrasmall mg nanoparticle anode," *Advanced Materials*, vol. 23, no. 5, pp. 640–643, 2010.

[30] J. Shuai, H. D. Yoo, Y. Liang, Y. Li, Y. Yao, and L. C. Grabow, "Density functional theory study of li, na, and mg intercalation and diffusion in mos2with controlled interlayer spacing," *Materials Research Express*, vol. 3, no. 6, p. 064001, 2016.

[31] W. Yuan and J. R. Gunter, "Insertion of bivalent cations into monoclinic nbs3 prepared under high pressure and their secondary batteries," *Solid State Ionics*, vol. 76, no. 3-4, pp. 253–258, 1995.

[32] Z. Rong, R. Malik, P. Canepa, G. Sai Gautam, M. Liu, A. Jain, K. Persson, and G. Ceder, "Materials design rules for multivalent ion mobility in intercalation structures," *Chemistry of Materials*, vol. 27, no. 17, pp. 6016–6021, 2015.

[33] T. D. Gregory, "Nonaqueous electrochemistry of magnesium," *Journal of The Electrochemical Society*, vol. 137, no. 3, p. 775, 1990.

[34] L. F. Wan, J. T. Incorvati, K. R. Poeppelmeier, and D. Prendergast, "Building a fast lane for mg diffusion in -moo3 by fluorine doping," *Chemistry of Materials*, vol. 28, no. 19, pp. 6900–6908, 2016.

[35] J. T. Incorvati, L. F. Wan, B. Key, D. Zhou, C. Liao, L. Fuoco, M. Holland, H. Wang, D. Prendergast, and K. R. e. a. Poeppelmeier, "Reversible magnesium intercalation into a layered oxyfluoride cathode," *Chemistry of Materials*, vol. 28, no. 1, pp. 17–20, 2015.

[36] G. Sai Gautam, P. Canepa, A. Abdellahi, A. Urban, R. Malik, and G. Ceder, "The intercalation phase diagram of mg in v2o5 from first-principles," *Chemistry of Materials*, vol. 27, no. 10, pp. 3733–3742, 2015.

[37] G. G. Amatucci, F. Badway, A. Singhal, B. Beaudoin, G. Skandan, T. Bowmer, I. Plitz, N. Pereira, T. Chapman, and R. Jaworski, "Investigation of yttrium and polyvalent ion intercalation into nanocrystalline vanadium oxide," *Journal of The Electrochemical Society*, vol. 148, no. 8, p. A940, 2001.

[38] G. Gershinsky, H. D. Yoo, Y. Gofer, and D. Aurbach, "Electrochemical and spectroscopic analysis of mg2+ intercalation into thin film electrodes of layered oxides: V2o5 and moo3," *Langmuir*, vol. 29, no. 34, pp. 10 964–10 972, 2013.

[39] R. Zhang and C. Ling, "Unveil the chemistry of olivine fepo4 as magnesium battery cathode," *ACS Applied Materials Interfaces*, vol. 8, no. 28, pp. 18 018–18 026, 2016.

[40] X. Chen, F. L. Bleken, O. M. Løvvik, and F. Vullum-Bruer, "Comparing electrochemical performance of transition metal silicate cathodes and chevrel phase mo 6 s 8 in the analogous rechargeable mg-ion battery system," *Journal of Power Sources*, vol. 321, pp. 76–86, 2016.

[41] Y. Orikasa, T. Masese, Y. Koyama, T. Mori, M. Hattori, K. Yamamoto, T. Okado, Z.-D. Huang, T. Minato, and C. e. a. Tassel, "High energy density rechargeable magnesium battery using earth-abundant and non-toxic elements," *Scientific Reports*, vol. 4, no. 1, 2014.

[42] P. B. Tchounwou, C. G. Yedjou, A. K. Patlolla, and D. J. Sutton, *Heavy Metal Toxicity and the Environment*. Basel: Springer Basel, 2012, pp. 133–164. [Online]. Available: https://doi.org/10.1007/978-3-7643-8340-4_6

[43] D. S. Sholl and J. A. Steckel, *Density functional theory: A Practical Introduction*. John Wiley Sons, 2009.

[44] A. Marthinsen, *Fundamentals and applications of density functional theory*, 2016. [Online]. Available: https://www.youtube.com/watch?v=SXvhDLCycxc

[45] M. M. Burbidge, "An introduction to vasp," 2014. [Online]. Available: http://hagrid.byu.edu/wiki/core/images/6/65/Matt_Learn_VASP.pdf

[46] *INCAR - cms.mpi.univie.ac.at*, 2019. [Online]. Available: https://cms.mpi.univie.ac.at/wiki/index.php/INCAR

[47] *KPOINTS - cms.mpi.univie.ac.at*, 2019. [Online]. Available: https://cms.mpi.univie.ac.at/wiki/index.php/KPOINTS

[48] *POSCAR - cms.mpi.univie.ac.at*, 2019. [Online]. Available: https://cms.mpi.univie.ac.at/wiki/index.php/POSCAR

[49] N. Van Landschoot, *Synthesis and characterization of inverse spinels, intercalation materials for Li-ion batteries*. Delft University of Technology, 2006. [Online]. Available: https://repository.tudelft.nl/islandora/object/uuid:3Ab76abcdd-1361-43c1-bcb4-9841e08c27ff

[50] *POTCAR - cms.mpi.univie.ac.at*, 2019. [Online]. Available: https://cms.mpi.univie.ac.at/wiki/index.php/POTCAR

[51] A. Rosen, "Vasp - rules of thumb." [Online]. Available: https://sites.tufts.edu/andrewrosen/density-functional-theory/vasp/

[52] S. L. Dudarev, G. A. Botton, S. Y. Savrasov, C. J. Humphreys, and A. P. Sutton, "Electron-energy-loss spectra and the structural stability of nickel oxide:an lsda+u study," *Physical Review B*, vol. 57, no. 3, pp. 1505–1509, 1998.

[53] [Online]. Available: https://cms.mpi.univie.ac.at/vasp-forum/viewtopic.php?t=2816

[54] [Online]. Available: https://wiki.fysik.dtu.dk/gpaw/tutorials/hubbardu/hubbardu.html

[55] A. Urban, D.-H. Seo, and G. Ceder, "Computational understanding of li-ion batteries," *npj Computational Materials*, vol. 2, no. 1, 2016.

[56] K. S. Yoo, N. W. Cho, and Y.-J. Oh, "Structural and electrical characterization of li(mn1ti)2o4 electrode materials," *Solid State Ionics*, vol. 113-115, no. 1-2, pp. 43–49, 1998.